

## INFORMATION TO USERS

This manuscript has been reproduced from the microfilm master. UMI films the text directly from the original or copy submitted. Thus, some thesis and dissertation copies are in typewriter face, while others may be from any type of computer printer.

**The quality of this reproduction is dependent upon the quality of the copy submitted.** Broken or indistinct print, colored or poor quality illustrations and photographs, print bleedthrough, substandard margins, and improper alignment can adversely affect reproduction.

In the unlikely event that the author did not send UMI a complete manuscript and there are missing pages, these will be noted. Also, if unauthorized copyright material had to be removed, a note will indicate the deletion.

Oversize materials (e.g., maps, drawings, charts) are reproduced by sectioning the original, beginning at the upper left-hand corner and continuing from left to right in equal sections with small overlaps.

ProQuest Information and Learning  
300 North Zeeb Road, Ann Arbor, MI 48106-1346 USA  
800-521-0600

UMI<sup>®</sup>



# Tumor Motion Problem During Radiotherapy Treatment

By  
Jilan Chen

A thesis submitted to  
the Faculty of Graduate Studies and Research  
in partial fulfilment of  
the requirements for the degree of  
Master of Computer Science

Ottawa-Carleton Institute for Computer Science  
School of Computer Science  
Carleton University  
Ottawa, Ontario

April 29, 2005

© Copyright  
2005, Jilan Chen



Library and  
Archives Canada

Bibliothèque et  
Archives Canada

0-494-06828-0

Published Heritage  
Branch

Direction du  
Patrimoine de l'édition

395 Wellington Street  
Ottawa ON K1A 0N4  
Canada

395, rue Wellington  
Ottawa ON K1A 0N4  
Canada

**NOTICE:**

The author has granted a non-exclusive license allowing Library and Archives Canada to reproduce, publish, archive, preserve, conserve, communicate to the public by telecommunication or on the Internet, loan, distribute and sell theses worldwide, for commercial or non-commercial purposes, in microform, paper, electronic and/or any other formats.

The author retains copyright ownership and moral rights in this thesis. Neither the thesis nor substantial extracts from it may be printed or otherwise reproduced without the author's permission.

**AVIS:**

L'auteur a accordé une licence non exclusive permettant à la Bibliothèque et Archives Canada de reproduire, publier, archiver, sauvegarder, conserver, transmettre au public par télécommunication ou par l'Internet, prêter, distribuer et vendre des thèses partout dans le monde, à des fins commerciales ou autres, sur support microforme, papier, électronique et/ou autres formats.

L'auteur conserve la propriété du droit d'auteur et des droits moraux qui protègent cette thèse. Ni la thèse ni des extraits substantiels de celle-ci ne doivent être imprimés ou autrement reproduits sans son autorisation.

---

In compliance with the Canadian Privacy Act some supporting forms may have been removed from this thesis.

Conformément à la loi canadienne sur la protection de la vie privée, quelques formulaires secondaires ont été enlevés de cette thèse.

While these forms may be included in the document page count, their removal does not represent any loss of content from the thesis.

Bien que ces formulaires aient inclus dans la pagination, il n'y aura aucun contenu manquant.

  
**Canada**

# Abstract

The goal of radiotherapy treatment is to kill a cancerous tumor while minimizing the damage to the surrounding healthy tissues. Several factors affect the ability to achieve this goal. One of the factors is tumor motion (e.g., as a result of breathing). In this thesis, we introduced a new solution to compensate for respiratory movement both for treatment planning and for treatment during radiation therapy. We also presented an algorithm which computes tumor coverage due to a patient's respiratory cycle. This algorithm solves the following problem: Given an  $n$ -vertex convex polygon  $P = \{v_1, v_2, \dots, v_n\}$  and a monotone chain  $C = \{c_1, c_2, \dots, c_m\}$ , compute a minimal area polygon  $Q$  that includes all the space covered by  $P$  as it is translated along  $C$  such that  $C$  is the trajectory of a vertex  $v_i \in P$ . Our algorithm takes  $O(mn + m \log n \log(m+n))$  time in the worst case. By applying this algorithm, individual tumor coverage can be computed and used to optimize treatment planning.

# Acknowledgements

I would like to express my sincere gratitude and appreciation to my supervisor, Dr. Doron Nussbaum for his guidance and support during this research.

I would also like to thank the physician working in ORCC, Dr. Miller MacPherson, for his advice, ideas, suggestions, and comments throughout the development of this thesis. His cooperation and guidance are highly appreciated.

Also, I would like to thank my defense committee: Dr. Amiya Nayak and Dr. Mark Lanthier for taking their time reading my thesis, and for their corrections and comments.

As well, I would like to thank all members of the PARADIGM group at Carleton University for their ideas and suggestions.

Last but not least, I would like to dedicate this thesis to my husband and my son who have always given me strength, encouragement, inspiration, and support.

# Acronyms and Definitions

- **CTV** – Clinical Target Volume: the volume of tissue that has to be treated to achieve local control of the cancer
- **DIBH** – Deep Inspiration Breath-Hold: one type of breathing holding techniques in radiation therapy with patient’s deep inspiration
- **DICOM** – Digital Imaging and Communications in Medicine: a standard for communications among medical imaging devices
- **DMLC** – Dynamic Multi-Leaf Collimator: a method used to deliver radiation using an MLC with the leaves in motion during radiation delivery
- **DRR** – Digital Reconstructed Radiograph: a projection of three dimensional CT scans that produces a “radiograph image”
- **GTV** – Gross Tumor Volume: the tumor visible in CT and other imaging studies
- **Gy** – (dose) Grays: units of measure for absorbed radiation dose
- **IMRT** – Intensity Modulated Radiation Therapy: a form of conformal radiation therapy with varied intensity of the radiation beam across the treatment field
- **OAR** – Organs At Risk: critical organs which are in close proximity to tumors and whose radiation sensitivity may significantly influence treatment planning
- **PTV** – Planning Target Volume: the geometrical expansion of CTV, which is designed to ensure full irradiation of the CTV by taking into all the uncertain factors such as tumor motion and setup error
- **ROI** – Regions Of Interest: the study area in the source images

# Contents

<b>Abstract</b>	<b>iii</b>
<b>Acknowledgements</b>	<b>iv</b>
<b>Acronyms and Definitions</b>	<b>v</b>
<b>1 Introduction</b>	<b>1</b>
1.1 Tumor Motion Problem . . . . .	2
1.2 Thesis Organization . . . . .	4
<b>2 Background</b>	<b>6</b>
2.1 Treatment Planning and Reporting Terminology . . . . .	6
2.2 Imaging Processing Techniques . . . . .	8
2.2.1 Digital Reconstructed Radiograph . . . . .	9
2.2.2 Image Registration . . . . .	13
2.3 Review of Previous Work . . . . .	18
2.3.1 Breath Holding Techniques . . . . .	20
2.3.2 Respiration Gated Radiotherapy . . . . .	22
2.3.3 Real-Time Tumor Tracking Radiotherapy . . . . .	24
2.3.4 Summary . . . . .	26
<b>3 Tumor Motion Compensation</b>	<b>27</b>
3.1 Overview . . . . .	29
3.2 Stage 1: Image Processing . . . . .	32

3.3	Stage 2: Tumor Coverage Computation . . . . .	34
3.4	Stage 3: Real Time Tumor Tracking . . . . .	36
<b>4</b>	<b>Path Polygon Algorithm</b>	<b>40</b>
4.1	The Tumor Coverage Problem . . . . .	40
4.2	Preliminaries . . . . .	41
4.3	Properties of the Path Polygon . . . . .	43
4.4	Algorithm . . . . .	46
4.4.1	Adding $P^i$ to $P^{1,i-1}$ . . . . .	46
4.4.2	Main Algorithm . . . . .	51
4.5	Summary . . . . .	53
<b>5</b>	<b>System Implementation</b>	<b>54</b>
5.1	Overview . . . . .	54
5.2	Coordinate Systems . . . . .	57
5.3	CT Images and Information Display . . . . .	59
5.4	DRR and Image Registration . . . . .	63
5.5	Tumor Coverage Computation . . . . .	67
5.6	DRR Testing . . . . .	69
<b>6</b>	<b>Conclusion</b>	<b>71</b>
	<b>Bibliography</b>	<b>74</b>
	<b>Appendices</b>	<b>81</b>
<b>A</b>	<b>CT Slice Information Dumping</b>	<b>81</b>
<b>B</b>	<b>RT Structure Information Dumping</b>	<b>84</b>
<b>C</b>	<b>RT Plan Information Dumping</b>	<b>89</b>

# Chapter 1

## Introduction

Statistics from the Terry Fox Research showed that in Canada cancer is the leading cause of premature death and primarily a disease of older people, particularly for men. The statistics also showed that lung cancer remains the leading type of cancer-related deaths for both sexes in 2004. Almost one-third of the cancer deaths in men, and almost one-quarter of the cancer deaths in women, are due to lung cancer alone [37]. For Canadian women, breast cancer is the most frequently diagnosed cancer. One in nine women is expected to develop breast cancer during her lifetime. One in twenty seven will die of it.

Radiation therapy uses high-energy radiation from X-rays, neutrons, and other sources to kill cancer cells and shrink tumors. The goal is to kill the cancerous cells while, at the same time, reducing the damage to the surrounding healthy tissues.

One of the biggest challenges for treating these types of cancer is the uncertainties such as setup error, organ motion, physical and geometric penumbra, etc. This is especially true for cancer located in the lungs, breasts and abdomens, where the related organs move rhythmically as a patient breathes. Imaging studies using fluoroscopy and ultrasound have shown that tumors located in these organs can move up or down several centimeters in some instances [26].

These facts and challenges motivated us to seek high precision radiotherapy and

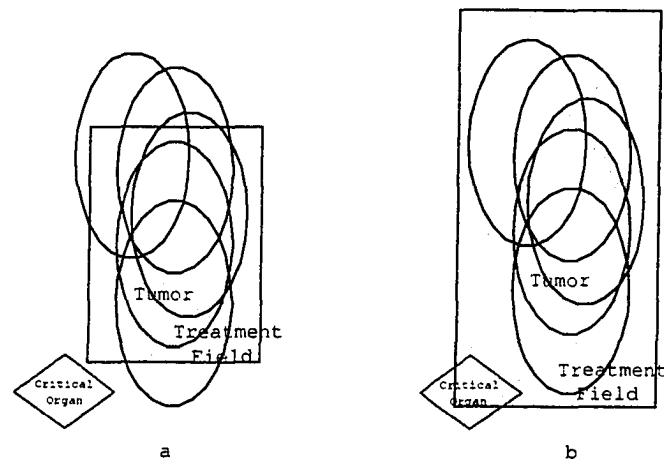


Figure 1.1: Tumor motion problem during radiation therapy.

focus our study on tumor motion problems caused by patients' breaths during treatment planning and treatment.

## 1.1 Tumor Motion Problem

It has been shown that a delivery of an increased amount of radiation dose to the tumor leads to a higher probability of killing the cancer. However, its downside is that critical organs and healthy tissues also receive an increased radiation. Some organs, near the tumor, may be very sensitive to an excess radiation dose and thus there is a risk of injury causing further medical complications [14].

As we described before, a tumor located in a lung, breast or abdomen can move a significant distance due to a patient's breathing. Usually, the respiration cycle is shorter than the time needed to deliver a treatment. Therefore, radiation treatment to the tumors located in these organs can be challenging due to the movement of the tumor target. The tumor image used during the treatment planning phase does not represent its true anatomical position, volume or shape during treatment [1].

This tumor motion problem is illustrated in Figure 1.1 a. The tumor is represented by an oval shape and it is located in different positions through the time of the treatment. Assuming that the tumor position (in red color) is used for treatment planning and the blue rectangle is designed as the treatment field, the problem occurs in two situations during treatment: (a) the treatment field may not cover the tumor completely and (b) the healthy tissue (or critical organ) around the tumor may be under radiation considerably. Both of them challenge the goal of radiation therapy and affect the curing of cancer patients.

Conventional treatment planning methods design the treatment field by adding a large margin (i.e., **safety margin**) to cover all the tumor motion during any time of a treatment. The consequence is that a significant volume of healthy tissue is exposed to radiation unnecessarily [35] (see Figure 1.1b). Moreover, as radiotherapy becomes increasingly conformal and tends to deliver higher doses over fewer fractions, the issue of tumor motion becomes more important. Haken [15] described that any change in the diameter of the treatment field will cause a big change in volume because the extended field is at the outside of the target volume that we are trying to treat. In some cases, a big margin may not be allowed since some nearby critical organs can be sensitive to excess radiation dosage and are at risk of being damaged, hence causing serious side effects [14].

In our approach, we study this tumor motion problem from a geometrical perspective. Our long term goal is to develop a non-invasive and efficient system to deliver radiation to a moving target during radiation treatment. We have made three contributions in this thesis.

Firstly, we suggest a new treatment process as the solution to compensate for tumor motion during radiation therapy. This new process aims at reducing the radiation dose to the healthy tissue and increasing the opportunity of killing the tumor by increasing the geometric matching between the tumor and the irradiation field. Efforts are made in two aspects: reducing the safety margin before treatment and monitoring the tumor movement during treatment. The medical industry can benefit

from our research in the area of treatment planning and treatment machine development because this technology may reduce the level of complication as a result of radiation treatment.

Secondly, we present a path polygon algorithm to compute a polygon's path coverage through its movement. This path polygon algorithm solves the following geometric problem: Given an  $n$ -vertex convex polygon  $P = \{v_1, v_2, \dots, v_n\}$  and a monotone chain  $C = \{c_1, c_2, \dots, c_m\}$ , compute a minimal area polygon  $Q$  that includes all the space covered by  $P$  as it is translated along  $C$  such that  $C$  is the trajectory of a vertex  $v_i \in P$ . Our algorithm takes  $O(mn + m \log n \log(m + n))$  time in the worst case. By applying this algorithm to the tumor's movement in our new process, tumor coverage, which represents all the region that the tumor passes during a patient's normal breathing, can be obtained and used as a reference or a guide for the physicians to design the treatment field.

Lastly, we develop an interactive software system to study the performance of our safety margin reducing process. This software system not only implements a variety of image processing algorithms such as digital reconstructed radiographs and image registration, but also integrates these algorithms together with our path polygon algorithm for clinical use. This system is written with visual C++ and can be executed on any Windows platform.

## 1.2 Thesis Organization

The rest of this thesis is organized as follows: Chapter 2 describes the background information of our research and gives a brief review of previous work in the area. Chapter 3 introduces the process flow of our new compensation solution, which enables physicians to take into account a patient's breathing movement during treatment planning and treatment. Chapter 4 presents our path polygon algorithm used to compute tumor coverage and gives the proof of its correctness. Chapter 5 introduces the software system we developed to study our new process and describes the detailed

functions included in this system. Chapter 6 summarizes the thesis and discusses possible improvements and future work.

# Chapter 2

## Background

As we described in Chapter 1, the motion of internal organs caused by breathing may greatly degrade the effectiveness and efficiency of radiation therapy during treatment. To deliver the prescribed radiation dose to the target volume of a moving tumor but avoiding the adjacent healthy tissues, investigators have developed several methods to reduce this targeting position error associated with this motion during treatment planning and treatment.

This chapter introduces several terms used for treatment planning and reporting, and then describes the image processing techniques used in radiation therapy. Finally, it reviews the previous work related to the tumor motion problem.

### 2.1 Treatment Planning and Reporting Terminology

Treatment planning is a very important first step in the radiation therapy process. It involves determining the position, angle and intensity of delivering radiation doses. The goal of planning is to make the treatment more precise, more effective, and less damaging to healthy tissues.

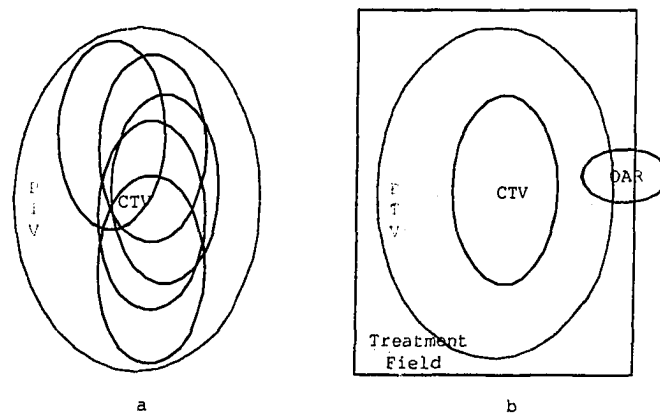


Figure 2.1: The PTV is the geometric expansion of the CTV.

For treatment planning and reporting, several terms were defined by the International Commission on Radiation Units and Measurements (ICRU) Report 50 [48]. This report provides guidelines for prescribing and reporting radiation therapy treatment. To facilitate our further discussion, we introduce these terms here.

The Gross Tumor Volume (GTV) is defined as “the gross palpable or visible/demonstrable extent of malignant growth text”. The GTV incorporates the tumor visible in CT and other imaging studies as well as known infiltration of lymph nodes and results from physical exams. It represents the volume of tumor area to be processed.

The Clinical Target Volume (CTV) is defined as “tissue that contains a demonstrable GTV and/or subclinical microscope malignant disease, which must be eliminated”. The CTV is designed to include cancer spread that cannot be seen in the CT scan or other imaging modalities. Often the delineation of the CTV relies on the medical judgement of physicians trained in specific treatment sites. The CTV represents the volume of tissue that has to be treated to achieve local control of the cancer.

Ideally, treatment plan should incorporate many different aspects of uncertainties in the planning and delivery stages of radiation treatment. The Planning Target

Volume (**PTV**) is defined as a geometrical expansion of the CTV and is designed to ensure full irradiation of the CTV by taking into all the uncertain factors such as tumor motion and setup error. Figure 2.1a shows that when a patient breathes, the tumor represented by the CTV can be located in different positions through out the treatment. Thus, the PTV must cover all the CTVs.

The Organs at Risk (**OARs**) are critical organs, which are in close proximity to tumors and whose radiation sensitivity may significantly influence treatment planning. Figure 2.1b shows that the OAR is under the irradiation due to the PTV's superfluous expansion.

As illustrated in Figure 2.1, provided an adequate margin, tumor coverage can be guaranteed with a high degree of certainty. However, enlarging the CTV region also means increasing radiation dose to healthy tissues, which conflicts with the main goal of radiation therapy. The selection of margin size can be very difficult, particularly because the methodology does not ensure that the dose delivered to these surrounding OARs is kept at an acceptable level [23]. As a result, the selection of the added margin size often involves a trade-off between assuring that the CTV receives the total dose and limiting the dose to the OARs.

During treatment planning, a radiation oncologist uses a process called *treatment simulation* to confirm that the treatment machine will treat the right location based on the prescribed treatment plan. A map of the area where the radiation is to be delivered, referred to as the *treatment field*, is created. Most patients have more than one treatment field. Different fields may be planned in the body's different positions.

## 2.2 Imaging Processing Techniques

Recent technical developments have advanced the capability of high precision radiation delivery. One of these techniques is to deliver intensity modulated beams, which is referred as Intensity Modulated Radiation Therapy (**IMRT**), using Dynamic Multi Leaf Collimator (**DMLC**) [14].

IMRT is an advanced mode of high precision radiotherapy that utilizes computer-controlled X-ray accelerators to precisely administrate radiation doses to a malignant tumor or specific areas within the tumor. IMRT radiation beams may consist of many very small beams in which each beam usually has a different intensity. On the receiving side, DMLC techniques can shape the field during irradiation and spare OARs that are very close to the target [50]. Thus, IMRT-DMLC techniques can map the radiation in such a way that the beams “wrap” around the tumor and conform to its shape to focus a higher radiation dose to the tumor while minimizing radiation exposure of surrounding normal tissues. However, this effort is challenged by tumor motion, especially the motion caused by patients’ breathing. When high radiation doses are used, tumor motion must be compensated and target error must be minimized during treatment in order to reduce damage.

In the sub sections to follow, we introduce two common image processing techniques used in our process to help analyze the tumor motion problem. One is Digital Reconstructed Radiograph, which is used to construct a simulated radiograph based on CT scans; and the other is Image Registration, which is used to obtain different information from different imaging modalities by aligning images.

### 2.2.1 Digital Reconstructed Radiograph

Digital Reconstructed Radiograph (**DRR**) is an important technique in clinical radio-oncology, defined as a projection of three dimensional CT scans that produces a “radiograph image”. This produced image (DRR) is widely used in radiotherapy treatment [4, 5, 25, 31, 34].

In general, DRR calculation methods are analogous to the physical process of producing radiographic films. To calculate a DRR, rays are traced from the position of the “virtual” X-ray source through the patient model to a point on a “virtual” film (see Figure 2.2). As each ray is traced, an estimation of radiographic attenuation (Formula 2.2) is obtained from the set of CT numbers associated with each CT voxel that the ray passes through. Illustrated in Figure 2.3, a voxel is defined as a cube with

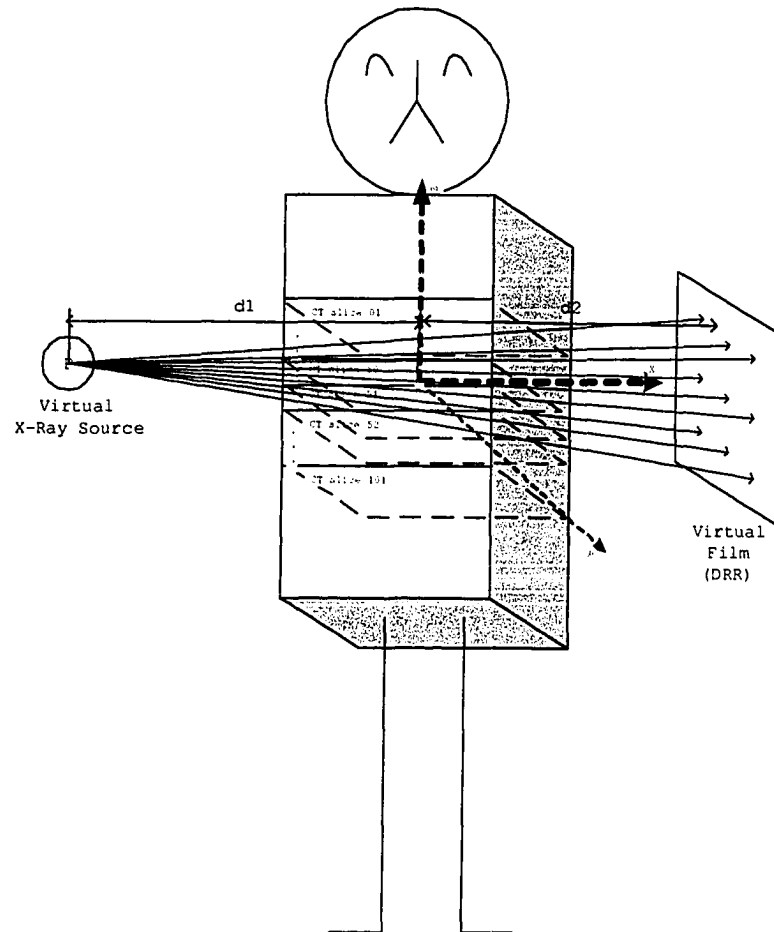


Figure 2.2: Simulated projection model for DRR.

eight adjoining pixels in two neighboring slices as its vertices. Then, the DRR pixel color can be determined based on the scale of this radiographic attenuation. In this section, we briefly summarize the three steps of a ray-casting algorithm [43] used in our process.

1) As shown in Figure 2.2, CT slices are cross sections of a patient model. This patient model can be divided into many voxels (Figure 2.3): the top and bottom planes of each voxel are formed by two neighboring slices; the four vertices of each plane are four adjoining pixels of each slice. Then, the length and width of this voxel

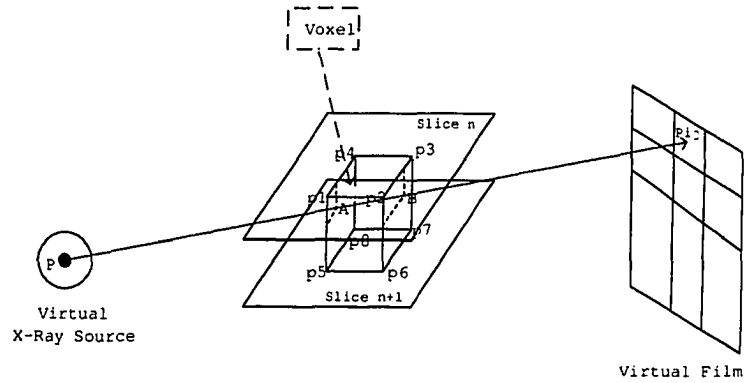


Figure 2.3: Ray casting algorithm.

is the same as the pixel space defined in each slice and its height is the thickness between two neighboring slices. It is possible that the voxel defined here may not be a cube but rather a box (width, length and height are not necessary to be the same).

2) For each projected ray, when it is generated from the X-ray source and travels through human tissue onto each pixel of the virtual film, it is separated into segments defined by the entrance (point A) and exit points (point B) for each voxel intersected by the ray (see Figure 2.3). For any intersected voxel  $k$ , its CT number  $CT_k$  at the segment midpoint can be represented by different options such as nearest neighbor and the average of its vertices. Then, its total linear attenuation coefficient  $U_k$ , which is the fraction of a beam  $k$  of x-rays absorbed or scattered per unit thickness of the absorber, can be computed through the following formula:

$$\left[ U_k = \frac{CT_k \times U_{water}}{1000} + U_{water} \right] \quad (2.1)$$

where  $U_{water}$  is the total linear attenuation coefficient of water for the same X-ray voltage and  $k$  is the index of the voxel. Water is used here as a reference to other materials since human body consists of water between the percentage of 60 to 80.

3) For each pixel  $p$  in the simulated film, when the ray travels from the X-ray

source to  $p$ , its relative beam attenuation can be estimated with an exponential attenuation expression (Equation 2.2) using the sum of products, that is the length of the separated segment  $D_k$  multiplied by the attenuation coefficient  $U_k$  (Equation 2.1) for each intersected voxel  $k$ .

Finally, the intensity  $I_p$  for each pixel  $p$  in the virtual film is

$$[I_p = I_0 \times e^{\sum(-U_k \times D_k)}] \quad (2.2)$$

where  $I_0$  is the original intensity of each ray,  $k$  is the index of each voxel through which the ray passes,  $U_k$  is the line attenuation coefficient of the material in voxel  $k$  and  $D_k$  is the segment between the entrance and exit points of the ray in voxel  $k$ .

For example, in Figure 2.3, we assume that the ray between  $P$  and  $p^{ij}$  only intersects with one voxel  $k$ . This voxel's CT number is 300 and the length of the intersected segment  $\overline{AB}$  is  $20mm$ . We also assume  $U_{water}$  is 0.021 and the ray's origin intensity is 1000 at point  $P$ . Based on Equation 2.1 and 2.2, we have:

$$I_p = 1000 \times e^{(-0.0273 \times 20)} \approx 579,$$

that means the ray intensity reduces to 579 when it reaches the point  $p^{ij}$ .

The above technique is described by the following pseudocode.

**Algorithm** RayCasting( $l$  of  $m \times n$  CT slices, X-ray source  $P$ ,  $s \times t$  DRR,  $I_0$ ,  $u_{water}$ )

{The function computes the ray value of all the pixels in DRR}

- 1: form a big voxel  $V$  by the boundary of  $l$  CT slices
- 2: divide  $l$  CT slices into  $(l - 1) \times (m - 1) \times (n - 1)$  small voxels
- 3: for each pixel  $p$  in DRR (total of  $s \times t$  pixels)
- 4: form the projected ray from point  $P$  to  $p$
- 5: if  $Pp$  intersects with the big voxel  $V$  then
- 6: find all the intersected small voxels
- 7: compute  $U_k$  by Equation 2.1 and  $D_k$  for each intersected voxel  $k$
- 8: compute the ray value of  $p$  by Equation 2.2

```
9: else {the projected ray only travels through air and the total attenuation coefficient is assumed to be 0}
10:    $I_p = I_0$ 
11: end if
endalgorithm
```

The simulated parameters such as radiation ISOcenter, which is usually the center-of-mass of the studied volume, ( $O$ ), Source-To-ISO distance ( $d1$ ), Source-To-Film distance ( $d1 + d2$ ), projected angle, etc. are based on the irradiated parameters of each treatment field from the treatment planning. The outcome is that each treatment position will have a corresponding DRR.

A DRR computed from CT scans used in computer-based simulation serves the same purpose as a radiograph from a conventional simulator. An advantage over conventional radiography is that the DRR provides a means for obtaining tumor contours, target volumes, and anatomical structures from CT scans. The DRRs computed by radiograph can be used as one source image in the process of image registration to transfer the useful information to another target image.

However, the quality of the DRR plays a very important role for its applications. Without a clear structure and accurate information of the observed targets such as tumor contour and bone structure, the produced DRR is difficult to use. DRR quality is influenced by a large number of parameters, including both details pertaining to the acquisition of the CT data as well as the specifics of the DRR calculation algorithm [8, 12, 22].

## 2.2.2 Image Registration

Image registration is an essential preprocessing step when using data from different data modalities and/or obtained at different times. Its task is to find a transformation from a coordinate system of one data set to another in order to ensure that all features that appear in both data sets are aligned. As we discussed above, a DRR computed by

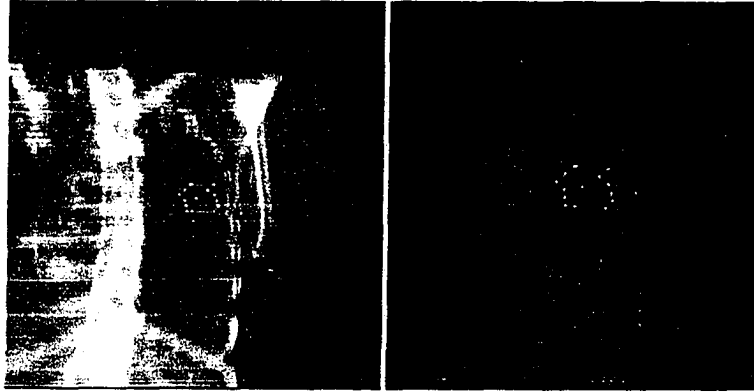


Figure 2.4: Tumor shape aligned in two different images.

radiograph can include the exact contour information of tumor and target volumes. On the other hand, fluoroscopic X-ray images can usually reveal tumor and organ movements but with a small field of view and limited resolution. Figure 2.4 shows a DRR in the left and a X-ray image in the right. The tumor shape in DRR (marked as yellow) is obtained from CTs and the tumor shape in X-ray image (marked as yellow) is registered from DRR. Combining information from DRRs and fluoroscopic X-rays, which is proposed in this thesis in order to analyze tumor movement, relies on image registration techniques which are described here.

Historically, different approaches have been developed for the registration of the DRR obtained from CT data to X-ray images [7, 19, 28]. These methods include using the features of image devices [3], the combination of intensity-based and point-based registration [40], fast-Fourier-transform-based cross-correlation [20] and gradient-based [27], etc. Alternatively, depending on how much of the original data is used to compute the transformation, these registration algorithms can be simply classified into two categories: geometry-based and intensity-based.

X-ray images have a limited resolution, orientation-dependent geometric and intensity distortions, and may also include some foreign objects. Therefore, most of the intensity-based registration algorithms are challenged with accuracy and speed. However, the features of some commonly identified structures (such as bone) can be

extracted both from the DRR and the X-ray radiograph. The two types of images can be aligned and matched by comparing these features. Then, the tumor information can be registered from the DRR into X-ray images under the assumption that the bone structure and the tumor are tied together. To simplify the registration process, the method discussed here is based on a geometrical registration algorithm with image landmark points on anatomical surfaces. These landmarks are often chosen as some joint points of the bone structure. Its process consists of three steps:

- 1) Identify landmarks by physicians in the source (DRR) and target (X-ray radiograph) image spaces;
- 2) Compute the corresponding transformation from the source image to the target image space;
- 3) Register tumor information using the derived transformation.

The first step is performed by physicians based on their experience. As long as the same landmarks can be identified in both images, step 2) can be performed as follows.

Let us assume that  $x_1, x_2, \dots, x_n$  and  $y_1, y_2, \dots, y_n$  are respectively the corresponding landmarks in the source and target image spaces. Since a DRR and an X-ray radiograph typically have different resolutions, we can find a  $2D$  transformation,

$$T(x_i) = \mathbf{sr}x_i + \mathbf{t}, \quad (2.3)$$

which maps  $x_i$  from the source space into the target space, where  $\mathbf{r}$  describes its rotation,  $\mathbf{s}$  describes its scaling and  $\mathbf{t}$  describes its translation. At least three landmark pairs are needed to solve this equation. Since there may be errors in the estimation of landmark positions, it would be beneficial to increase a accuracy in computing the transformation parameters by using more than three points. To find the registration parameter that better matches the source landmarks to the target landmarks, we minimize the sum of square residual errors:

$$\sum_1^n |T(x_i) - y_i|^2 \quad (2.4)$$

with respect to the unknowns  $\mathbf{s}$ ,  $\mathbf{r}$  and  $\mathbf{t}$ .

A simple algorithm [7] to find these transformation parameters can be described as follows:

**Algorithm** FindTransformation( $x_i, y_i$ )

{The function finds  $\mathbf{r}$ ,  $\mathbf{s}$  and  $\mathbf{t}$  to minimize the registration error}

- 1: Compute the centroid of the body representing the set of landmarks in each space as:

$$\begin{aligned} \tilde{x} &= \sum_1^n x_i/n \\ \tilde{y} &= \sum_i^n y_i/n \end{aligned}$$

- 2: Compute the displacement from the centroid to each landmark in each space:

$$\begin{aligned} \tilde{x}_i &= x_i - \tilde{x} \\ \tilde{y}_i &= y_i - \tilde{y} \end{aligned}$$

- 3: Compute the covariance matrix  $H$ :

$$H = \sum_1^n \tilde{x}_i \tilde{y}_i^t$$

where the superscript  $t$  indicates transpose of the original matrix. Therefore,  $H$  is a  $2 \times 2$  matrix since  $\tilde{x}_i$  is a  $2 \times 1$  matrix and  $\tilde{y}_i^t$  is a  $1 \times 2$  matrix.

- 4: Perform Singular Value Decomposition of  $H$ :

$$H = U \Lambda V^t$$

where  $U$  and  $V$  are both  $2 \times 2$  square matrix and both of which have orthogonal columns so that

$$U^t U = V^t V = I$$

and  $\Lambda$  is a  $2 \times 2$  diagonal matrix,  $\Lambda = \text{diag}(\lambda_1, \lambda_2)$ , and  $\lambda_1 \geq \lambda_2 \geq 0$ .

- 5:  $\mathbf{r} = V \text{diag}(1, \det(VU)) U^t$
- 6:  $\mathbf{s} = \sum_1^n (\mathbf{r} \tilde{x}_i) \cdot \tilde{y}_i / \sum_i^n (\mathbf{r} \tilde{x}_i) \cdot \tilde{x}_i$
- 7:  $\mathbf{t} = \tilde{y} - \mathbf{s} \tilde{x}$

**endalgorithm**

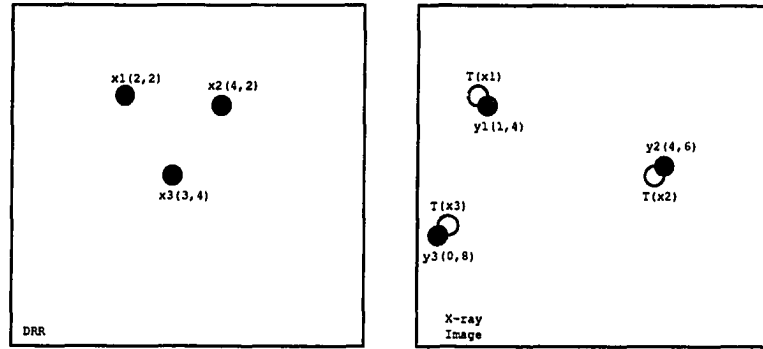


Figure 2.5: Landmark-based registration and its error.

The singular value decomposition of the matrix  $H \in \mathbb{R}^{2 \times 2}$  in Step 4 can be constructed by the following steps:

1. Find the eigenvalues of the matrix  $H^t H$  and arrange them in descending order as  $\lambda_1, \lambda_2$ .
2. Find the number of nonzero eigenvalues of the matrix  $H^t H$  as  $\gamma$ .
3. Find the orthogonal eigenvalues of the matrix  $H^t H$  corresponding to the obtained eigenvalues, and arrange them in the same order to form the column-vectors of the matrix  $V \in \mathbb{R}^{2 \times 2}$ .
4. Form a diagonal matrix  $\Lambda \in \mathbb{R}^{2 \times 2}$  placing on its diagonal with the square roots  $\delta_i = \sqrt{\lambda_i}$  of the eigenvalues got in Step 1 in descending order.
5. Find the two column-vectors of the matrix  $U \in \mathbb{R}^{2 \times 2}$ :  $u_i = \delta_i^{-1} H v_i$ .

After executing the above registration algorithm, any point  $x$  in the source space can be transformed into the target space by using the same transformation of  $T(x)$ .

To illustrate this algorithm, Figure 2.5 shows three landmarks in both DRR and X-ray images. Suppose  $x_1 = (2, 2), x_2 = (4, 2), x_3 = (3, 4)$  and  $y_1 = (1, 4), y_2 = (4, 6), y_3 = (0, 8)$ . Based on the algorithm of *FindTransformation*, we can compute:

$$\begin{aligned} \mathbf{s} &= 1.85, \\ \mathbf{r} &= \begin{pmatrix} 0.80 & 0.61 \\ -0.61 & 0.90 \end{pmatrix}, \\ \mathbf{t} &= \begin{pmatrix} 0.25, & -1.27 \end{pmatrix}. \end{aligned}$$

Applying this transformation on  $x_i$  with Equation 2.3, we get:

$$\mathbf{T}(x_1) = (0.94, 3.90),$$

$$\mathbf{T}(x_2) = (3.88, 6.14),$$

$$\mathbf{T}(x_3) = (0.18, 7.96).$$

The above algorithm assures that the registration error  $\sum_1^3 |T(x_i) - y_i|^2$  is minimized. For the tumor contour in DRR, its location in the X-ray image can be obtained by applying the same transformation to each of its points.

## 2.3 Review of Previous Work

Over the last decade, many researchers have investigated techniques and methods to overcome the uncertainties in radiation therapy. Koste et. al. [25] presented a procedure for executing a verification and correction step in order to reduce systematic setup errors using CT-Simulations and DRR. Hadley [14], Ezz et. al. [9], and Gerg et. al. [13] developed video-based imaging systems to measure patient location. Killoran et. al. [23] provided a numerical simulation to assess the CTV coverage and critical organ dose as a function of treatment margins in the presence of organ motion and physical setup errors. Many others [1, 11, 18, 29, 47] focussed specifically on respiratory movement due to its significant effect to internal anatomy.

In this section, we only discuss some typical methods which were developed to reduce or monitor tumor motion caused by respiratory movement. Note that although

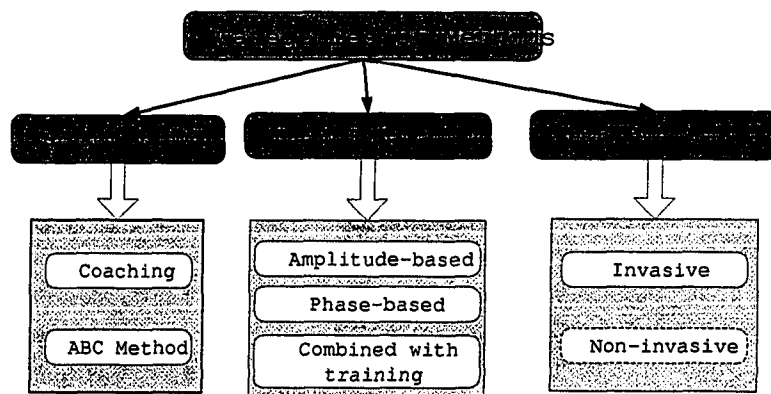


Figure 2.6: Categories of tumor motion related methods.

the reduction of the PTV margin is generally desirable, it should always be accompanied by an assurance that the risk of geometric misses (regions of tumor which are outside of the treatment field) does not also increase [51]. Therefore, the aim of these methods is to reduce the safety margin from the CTV to the PTV with efforts to provide maximum increase of the radiation dose to the CTV during treatment.

These methods can be categorized into three groups (see Figure 2.6). The simplest approach is to minimize the motion itself and the simplest way to achieve it is by breath-holding, which is discussed in Section 2.3.1. Instead of regulating the patient's breathing, one can synchronize the external beam exposure with the part of the breathing cycle where tumor motion is minimal, which is called respiratory gated radiotherapy and is discussed in Section 2.3.2. An arguably better but also more difficult approach is to allow the patient to breath freely while a tracking and control system monitors the tumor's position and adapts the alignment of the radiation field continuously to follow the moving target, which is called real-time tumor tracking radiotherapy and is described in Section 2.3.3. The later two strategies (the respiratory gating and real-time tracking) require a means of continuously observing or inferring the respiratory signal or the tumor position during treatment.

### 2.3.1 Breath Holding Techniques

In these breath holding techniques, the patient's breathing is controlled either by speaking to the patient (**coaching**) or by using an Active Breathing Control (**ABC**) apparatus machine.

The coaching method is simply to ask the patient to hold his/her breath at the end of deep or full inspiration to reduce lung density and to immobilize organs during radiation exposing. This method avoids the need for complex control of the machine. However, the patients usually need to be trained to hold their breaths. Not all patients may be suitable for this technique due to their health status. In a single session, patients need to perform 10 – 13 breath-holds for a duration of 12 – 16 seconds. A patient can easily feel tired and uncomfortable after a while. The effect of this method depends on the ability to reach and maintain total lung capacity voluntarily.

Hanley et. al. [16] evaluated the dosimetric benefits of a Deep Inspiration Breath-Hold (**DIBH**) technique in the treatment of lung tumors. He observed that the DIBH technique can reduce the volume of lung receiving doses more than 25 dose grays (**Gy**) by 20 percent compared to free-breathing plans. Rosenzweig et. al. [39] investigated the level of dose in which patients could be treated with DIBH. They observed that the dose level increased, on average, from 69.4Gy to 87.9Gy, without increasing the risk of toxicity.

Another breathing control technique is the ABC apparatus machine (see Figure 2.7 [51]). An ABC apparatus consists of 2 pairs of flow monitor and scissor valves, each one to control the inspiration and expiration paths to the patient. The patient breathes through a mouthpiece connected to the ABC apparatus. The respiratory signal is processed continuously to display the changing volume in real-time. At some point after the patient achieves a stable breathing pattern, the operator activates the ABC at a pre-selected point in the breathing cycle. Both valves are then closed to immobilize breathing motion. The period of active breath-holding is that which can be comfortably and repeatedly tolerated by each individual patient, as determined during a training session. Radiation will be turned on and off during this period. An

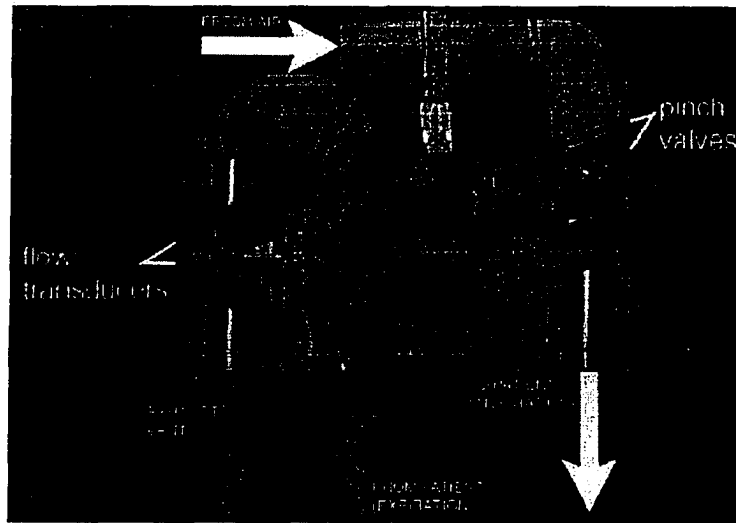


Figure 2.7: ABC apparatus machine.

ABC provides a simple means to reproducibly minimize breathing motion within the patient's tolerance. However, it still requires patients to hold their breaths during treatment.

Wong et. al. [51] studied the use of ABCs to reduce the safety margin of PTV for breathing motions. They indicated in their studies that with ABC, the excursions of a target center parameters for the livers were less than  $1mm$  at the same respiratory phase, but were larger than  $4mm$  at the extremes of the breathing cycle. Cheung et.al.[6] specified their studies with lung tumors. They concluded that with the use of ABC inspiration breath hold, the average ( $\pm$  standard deviation) displacement of GTV centers was  $0.3mm$  ( $\pm 1.8mm$ ),  $1.2mm$  ( $\pm 2.3mm$ ), and  $1.1mm$  ( $\pm 3.5mm$ ) in the lateral direction, anterior-posterior direction, and superior-inferior direction, respectively. Remouchamps et. al.[36] reached their conclusion that heart and lung doses can be significantly reduced using DIBH with ABC and IMRT techniques for loco-regional breast irradiation.

### 2.3.2 Respiration Gated Radiotherapy

In this approach, a patient is breathing freely but the patient's breathing is monitored by using a variety of devices. Based on respiratory signals, a short burst of radiation can be delivered repeatedly at a particular phase of the breathing cycle. This method requires real-time monitoring of the patient's breathing and real-time control of the radiation output.

Kubo et.al.[26] investigated the technical aspects of gating the radiotherapy beam synchronously with respiration. Their studies covered the optimal respiration monitoring system, measurements of organ displacement and the feasibility of linear accelerator gating. They examined several respiration sensors including a thermistor, a thermocouple, a strain gauge and a pneumotachograph; and concluded that the temperature sensor and strain gauge methods produced the most desirable signals among them: reproducible, accurate, quickly responding, comfortable and having a large signal-to-noise ratio. They also found that fluoroscopic images were extremely useful for determining the magnitude and direction of organ motion. The experienced results of the gated output, symmetry and uniformity measurements with the radiation treatment machine of "Varian 2100C" showed that gating did not change the beam characteristics.

Minohata et.al.[32] developed a gated irradiation system for heavy-ion radiotherapy. They argued that most of the commercial sensors available in the medical field were not easy to set up on patients during treatment and that signals from the sensors were not very stable. They used their own sensing system, which consisted of a Position-sensitive Semiconductor Detector (PSD), a PSD camera and an infrared light-emitting diode (ir-LED). The PSD camera detected any change in the ir-LED position. Then, the change in the position was amplified by the camera's zoom lens and the PSD analog output signalled in direct proportion to the spot position without any software. By applying a threshold to the respiration waveform, the gate signal used to request the beam was set around the end of the expiratory phase. Their performance test using a moving phantom found that this gated system could reduce

the target margin to 5 – 10mm although the target moved twice or three times.

Ford et. al.[11] evaluated the effectiveness of a commercial camera-based system: the Real-time Position Management system (**RPM**) from Varian Medical Systems in gating the radiation delivery . In the RPM gating system, a small plastic block with two infrared reflective markers were placed on the patient's chest. The markers were illuminated by infrared emitting diodes, and the resulting images were captured by a camera and digitized. The software tracked the position of the top marker; and the separation between the top and bottom markers provided a distance calibration. The system provided two modes of operation based either on the phase of the breathing cycle or on the trace amplitude. In amplitude-based gating, the minimal and maximal limits, between which the dose delivery was to occur, were defined. In phase-based gating, the system calculated the phase using a running estimate of the breathing period; and the user specified a range of phases during which the treatment beam would be enabled. This gating system also consisted of an algorithm that determined whether the respiration was regular. If this predictive breathing filter was enabled, the system turned off the gate signal at times of irregular breathing. This gating system was found to be able to reduce both inter- and intra-fraction variability of anatomy due to respiratory motion between 2.6mm and 5.7mm and between 0.6mm and 1.4mm, respectively.

Kini et.al.[24] evaluated the feasibility of combining patient training tools into the above RPM gating system. The training tools included audio prompting, which used instructions to “breathe in” or “breathe out” at periodic intervals deduced from the patients' own breathing patterns, and visual feedback, in which patients were shown a real-time trace of their abdominal wall motion due to breathing and were asked to maintain a constant amplitude of motion. They concluded that training tools improved the reproducibility of amplitude and frequency of patient breathing cycles.

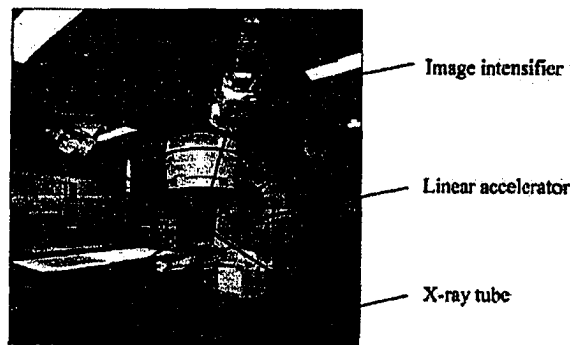


Figure 2.8: Shirato's fluoroscopic real-time tumor tracking system.

### 2.3.3 Real-Time Tumor Tracking Radiotherapy

Distinguished from the above methods of gating external breathing signals, real-time tumor tracking radiotherapy pursues a means to observe a tumor's movement and locate its position continuously in order to adjust beam fields dynamically.

Shirato et.al.[46] developed a linear accelerator synchronized with a fluoroscopic real-time tumor tracking system (See Figure 2.8). During treatment planning, a 2 – mm gold marker was inserted into the tumor or placed near the tumor to be detected by a CT scan for treatment planning. During treatment, coordinates of the tumor center and the gold marker are transferred to the fluoroscopic real-time tumor tracking system. By comparing the dislocation between the moving gold marker and the tumor center with the predetermined value, the computer was able to recognize that the motion pattern of the gold marker was less than satisfactory. This resulted in the tracking system preventing the linear accelerator from irradiating the patient. Otherwise, the system allows the linear accelerator to irradiate the patient. The results in their phantom experiment showed that the 3D location of this inserted marker could be determined with an accuracy of  $\pm 1mm$  every 0.033 seconds during radiotherapy and that dose distribution was much more accurate by using the fluoroscopic real-time tumor tracking system.

In the relative studies afterward, this real-time tumor tracking system was being used or checked in different aspects. Shimizu et.al.[44] investigated the three-dimensional movement of lung tumors by using this real-time tumor tracking system. They obtained results showing that the range of marker movement during the “beam-off” period was  $5.5\text{mm} - 10.0\text{mm}$  in the lateral direction (x),  $6.8\text{mm} - 15.9\text{mm}$  in the crania-caudal direction (y) and  $8.1\text{mm} - 14.6\text{mm}$  in the ventro-dorsal direction (z). The range during “beam-on” period was reduced to within  $5.3\text{mm}$  in all directions. Harada et. al.[17] evaluated this tracking system for lung carcinoma treatment. They concluded that most peripheral-type lung tumors could be successfully treated using this system but it was not feasible for central-type lung tumors. Shirato et. al.[45] examined the feasibility of inserting fiducial markers into various organs with different equipment and techniques respectively. Sharp et. al.[42] tried different predictive models to reduce tumor localization errors caused by a slow imaging rate and large system latencies while using this system.

Schweikard et.al.[41] suggested to compensate for respiratory motion by moving the radiation beam with a robotic arm and following the moving target tumor. To determine the precise position of the moving target, infrared emitters were used to record the motion of the patient’s skin surface and a synchronized X-ray imaging system could provide information about the location of internal implanted markers. Their results showed that robot-based methods could substantially reduce the safety margins currently needed in radiation therapy.

Regarding the delivering of the dose to a moving target, Keall et. al. [21] proposed a solution of adapting the X-ray beam using a dynamic multi-leaf collimator. During beam delivery, the beam was dynamically changing position with respect to the isocenter using a dynamic MLC, the leaf positions of which were dependent upon the target position. They investigated the feasibility of delivering such a treatment in their studies. They assumed that the patient’s breathing was regular and reproducible (only sinusoidal motion was used for their experiments).

### 2.3.4 Summary

In summary, previous work related to tumor motion problems can be grouped into three categories: breathing holding techniques, gated radiation therapy, and real-time tracking methods. Breathing holding techniques either control a patient's breathing by coaching and/or by using an ABC machine so that tumor motion can be reduced during treatment. Both of them require patients' training. Patients need to hold their breaths through out each treatment. These methods are simple but patients easily feel tired.

Respiration gated radiotherapy monitors breathing by using a variety of devices and gates beams on/off automatically based on patients' respiratory cycle. Under this approach, a patient can breath freely but the patient's breathing is monitored by a variety of sensors. Based on respiratory signals, a short burst of radiation is delivered repeatly at a particular phase of the breathing cycle. This method requires real-time monitoring of the patient's breathing and real-time control of the radiation output.

Real-time tumor tracking radiotherapy uses a real-time tumor tracking system to synchronize a treatment machine with a patient's breathing. It pursues a means to observe a tumor's movement and locate its position continuously in order to adjust beam fields dynamically. The major shortcoming of the existed methods for this technique is its invasive.

The new approach we propose in this research is similar to real-time tumor tracking radiotherapy in terms of dynamically monitoring the tumor's motion, but distinguishes itself by being non-invasive objects required.

# Chapter 3

## Tumor Motion Compensation

This chapter introduces a non-invasive, geometry-based process as a solution to compensate for the tumor motion problem during radiation therapy. The goal of this process is to increase the matching region between the tumor and the treatment field in order to maximize the dose delivered to a tumor and to minimize the dose to the surrounding normal tissue. This goal is achieved by two sub-processes: pre-treatment tumor coverage analysis and intra-treatment, non-invasive tumor tracking. By analyzing each individual patient's tumor coverage before treatment, the required safety margin could be reduced and tightened to the target volume. By tracking the external skin markers during treatment, the patient's actual tumor movement could be correlated and the tumor's location could be dynamically identified without any invasive object.

As indicated in Chapter 2, the patterns of breathing motion can be complex, variable, and individualistic. The motion of internal organs caused by breathing is also influenced by cardiac beating, aortic pulsing, etc. Sometimes, this motion can be very unstable and hard to predict. It is very difficult to reach the necessary accuracy for cancer treatment if we don't compensate for this breathing movement. With increasing improvement in the advanced techniques such as IMRT, DMLC, imaging acquisition and processing, more and more compensation methods are becoming

possible and practical.

A typical cancer patient is usually treated 5 days per week over a period of six to eight weeks. Each treatment lasts a few minutes. Technologies such as breath-hold techniques may be poorly tolerated by pulmonary compromised patients and cause patients' hyperventilation, while directly tracking implanted external markers has a major shortcoming of being invasive regardless of whether for gated radiotherapy or real-time tracking. On the other hand, there are three critical issues that need to be considered for the respiratory gated radiotherapy no matter which sensor being chosen. First, the location of the sensor should be chosen carefully, which significantly influences the performance of the sensor signal for patients' respiration. Second, since the respiration waveform is an indirect signal of the organ motion, the phase difference between them must be examined. Third, the "gate-on" time should be determined carefully since shortening the "gate-on" period causes a better dose distribution, but also increases the treatment time.

In order to resolve the above shortcomings of current methods, our research pursues a freely-breathing and non-invasive solution to compensate for tumor motion during treatment planning and treatment. Our solution is similar to real-time tumor tracking radiotherapy in terms of dynamically monitoring a tumor's movement and locating its position. The major advantage of our solution is that it does not require "markers" to be placed inside a patient's body, which also distinguishes our solution from real-time tumor tracking radiotherapy.

The solution we propose here potentially benefits such cancer patients, whose tumors are non-stationary during treatment. By applying modern image processing techniques and various geometry algorithms into medical systems, we ultimately obviate some unnecessary side-effects of radiation therapy for these cancer patients.

In the following sections, we first introduce the principles of our compensation solution and the three stages included therein. We then describe each step in detail.

## 3.1 Overview

Different medical imaging modalities provide specific information that is used in various stages during the cancer treatment process. Due to the unique techniques of the image modalities, the required exposure time and the quality of the acquired images also vary.

CT scanning is used for most cancer patients to diagnose, locate the exact position of the tumor, and to compute the amount of absorbed radiation. Current CT scanners can acquire 32 image slices per second. A spiral scan can usually be obtained during a single breath hold. This allows scanning of a chest or an abdomen in 10 seconds or less. Since a scan usually performs 1 – 3 times during treatment and the scanning speed makes it possible for patients to hold their breath during CT scanning. This results in CT slices that are not affected by the breathing cycle. Alternate methods gate the CT imaging and obtain slices only during the same part of the breathing cycle from slice to slice. These techniques allow us to assume that CT slices can be taken without any movement of patients' organs or in the same phase of patients' breathing. After CT scanning, tumor contours and other target volume contours can be identified in each CT slice. These contour structures provide the basic tumor information for the process of our solution.

Each patient needs to undergo fluoroscopy with different treatment positions during simulation time. A video-camera system is set up to record fluoroscopic video from these positions. These videos are composed of a series of ordered X-ray radiographs, which reveal a tumor's movement caused by the patient's breathing but with a poor quality of soft tissues. Therefore, it is very difficult to identify tumor's shape directly in X-ray radiographs.

As illustrated in Figure 3.1, the process of our solution includes three stages. Before the process, the two types of images (CT scanning and fluoroscopy) discussed above can be acquired during the routine diagnosis and simulation phases of cancer treatment. This pre-processing step provides the input data to the first stage of our process and is called as **Image Acquisition**.

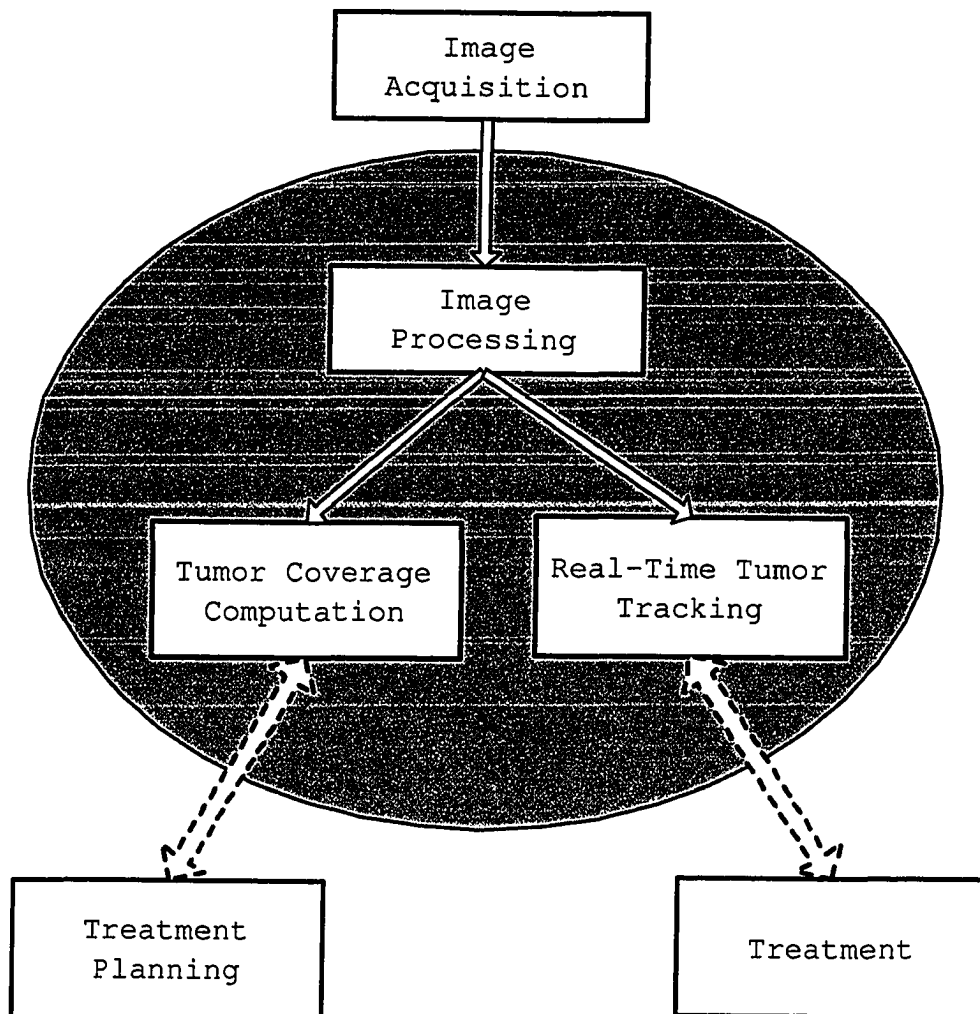


Figure 3.1: Three stages of the tumor motion compensation solution.

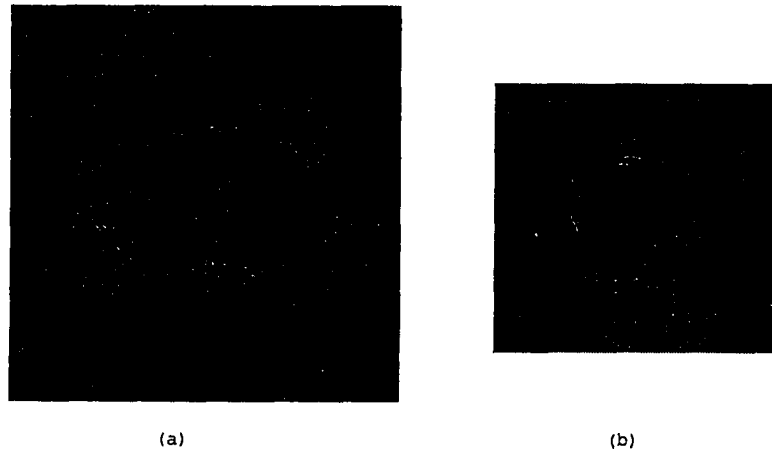


Figure 3.2: (a) A CT scan image and (b) a fluoroscopy image.

**Stage 1 – Image Processing** obtains tumor motion information by processing a patient’s CT scanning and fluoroscopy images (see Figure 3.2). Using DRR and image registration techniques described in Chapter 2, we are able to transfer tumor information from CT slices to X-ray radiographs to get the recording of tumor motion for each treatment field. The recording of individual tumor motion under a patient’s normal breathing provides the basic information for the analysis and computation of later stages.

**Stage 2 – Tumor Coverage Computation** computes tumor coverage, which is the expected region that the CTV may pass due to the tumor’s movement, by using a path polygon algorithm. Using the path polygon algorithm, the tumor is outlined as a simple polygon and the tumor’s movement is represented by many directed segment chains. The computed tumor coverage is used to verify and possibly reduce the PTV’s safety margin around the tumor. This tight matching of PTV with CTV may be used to increase the amount of dose to the tumor and possibly decrease the amount of dose to the healthy tissue and surrounding OARs.

**Stage 3 – Real Time Tumor Tracking** correlates the movement of the internal tumor with the external skin markers and then locates the tumor’s position during

treatment by monitoring the external skin markers. With the known location of the internal tumor, we can gate the irradiation by comparing it with the treatment field or simply move the patient's couch to compensate for tumor motion and focus the beam on the tumor.

Stage 2 is applied during the phase of treatment planning while Stage 3 is applied during the phase of treatment. To our best knowledge, the processes described in our approach are the first attempt to integrate these technologies together into a single system and apply them in the area of radiation therapy.

## 3.2 Stage 1: Image Processing

During this stage (see Figure 3.3), a patient is first scanned by a CT scanner and the CTV contour is outlined manually by a radiation oncologist on CT slices. Beam plans are also scheduled for different irradiation positions. Based on the data of CT slices, a DRR is reconstructed by using the algorithm described in Chapter 2 and a CTV contour is geometrically projected from 3D CTs to this DRR plane. To be consistent with the treatment positions, the same irradiation parameters are used to reconstruct each DRR for each beam position. In the final DRR image, we can see both the region of influence of each CT slice and the region of the tumor.

Secondly, a series of X-ray radiographs are extracted from a fluoroscopic video which is taken by a camera during simulation. The DRR and the X-ray radiographs are constructed from the same orientation and position of the treatment machine. Thus, the 2D image registration algorithm described in Chapter 2 can be used to register the CTV information from the DRR to the X-ray radiograph. In this step of our process, the used landmarks can be some commonly identified features (such as bone joint points) both in the DRR and the X-ray radiograph. By comparing these features, the two types of images can be aligned and matched. Then, the CTV contour can be registered from the DRR into X-ray images under the assumption that the bone structure and the tumor are moving synchronously. As long as we get

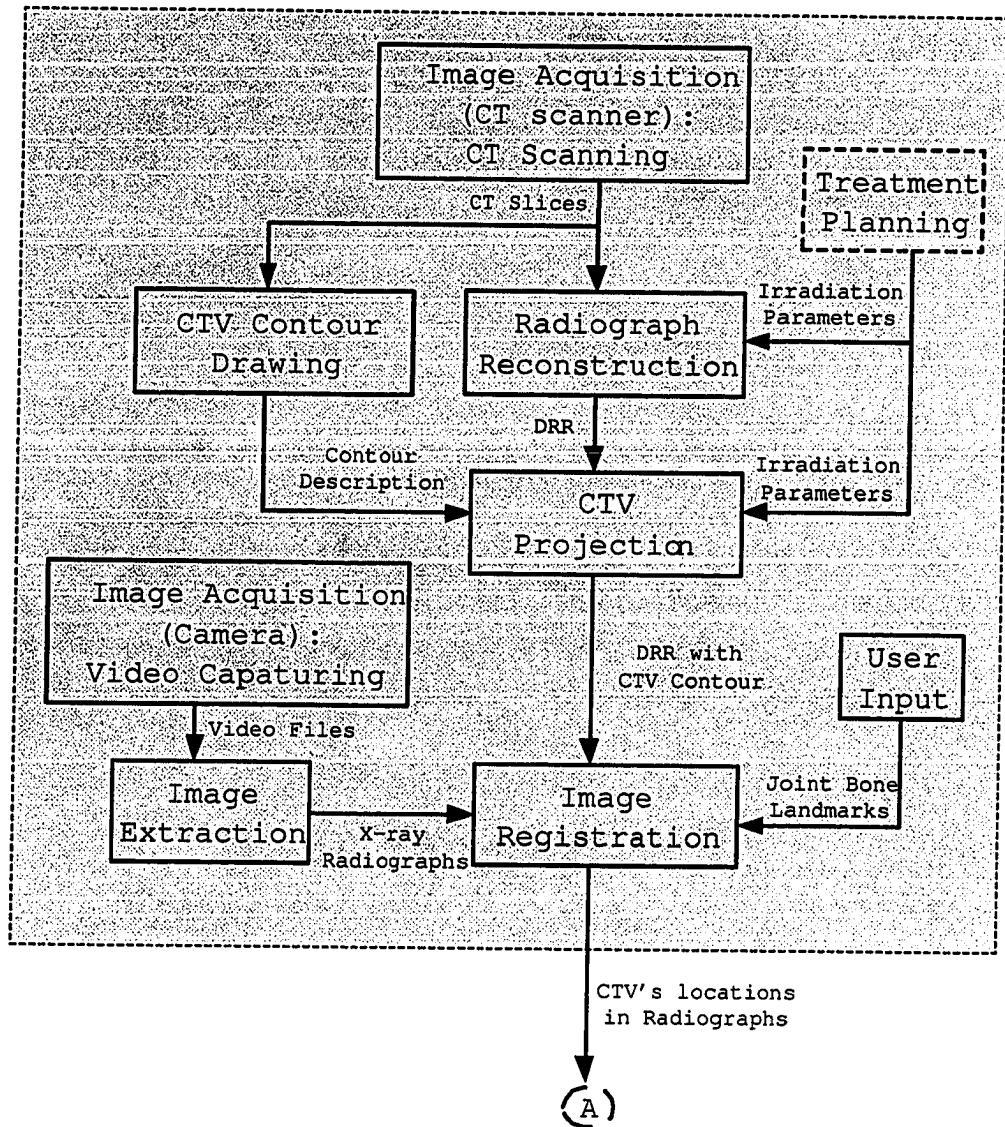


Figure 3.3: Images acquisition and processing.

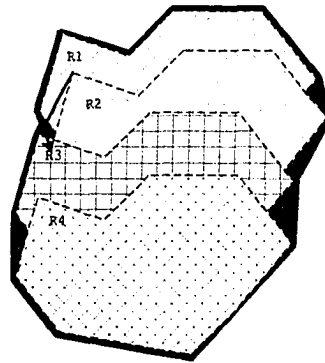
the tumor location in one X-ray image, we could manually or automatically detect the tumor positions in all other X-ray images. The outcome of this stage is a series of X-ray radiographs with identified CTV locations, which represent the movement of the tumor and are the input of the next two stages.

### 3.3 Stage 2: Tumor Coverage Computation

During this stage, the tumor's trajectory can be traced and the tumor motion coverage of a patient is computed based on the series of CTV locations within the X-ray radiographs from the previous stage.

The X-ray radiographs are taken with high frequency during simulation before treatment. These radiographs capture the movements of a patient's organs and tissue. From stage 1, the CTV location can be obtained accurately in each X-ray radiograph. Putting these radiographs in the order of time stamping, we can assume between each two consecutive radiographs, the movement is straight-headed from the first position to the second position. Then, the tumor's movement path can be formed by the chain of its discrete positions connected from the beginning to the end. Its coverage not only includes the union of tumor regions in different positions but also includes its movement path between each consecutive position. Figure 3.4 shows four consecutive tumor positions in four radiographs and the red arrows represent the moving directions of the extreme vertex from  $R1$  to  $R2$ ,  $R2$  to  $R3$ , and  $R3$  to  $R4$ . The region outlined with the blue line is the tumor coverage taking into account the tumor's movement. The small regions with green color are the difference between the tumor coverage and its union.

As illustrated in Figure 3.5, the path polygon algorithm (which is introduced in Chapter 4) takes these radiographs as input and computes the tumor coverage based on the CTV information within them. The tumor coverage represents the expected region that the tumor passes due to its respiratory movement during treatment. Physicians could use it to verify and potentially optimize the PTV. By comparing



- R1, R2, R3, R4 represent 4 consecutive tumor positions in 4 radiographs, respectively
- The moving direction of tumor between two consecutive radiographs
  - The difference between the overlap of tumors and its coverage

Figure 3.4: Tumor moving and coverage regions.

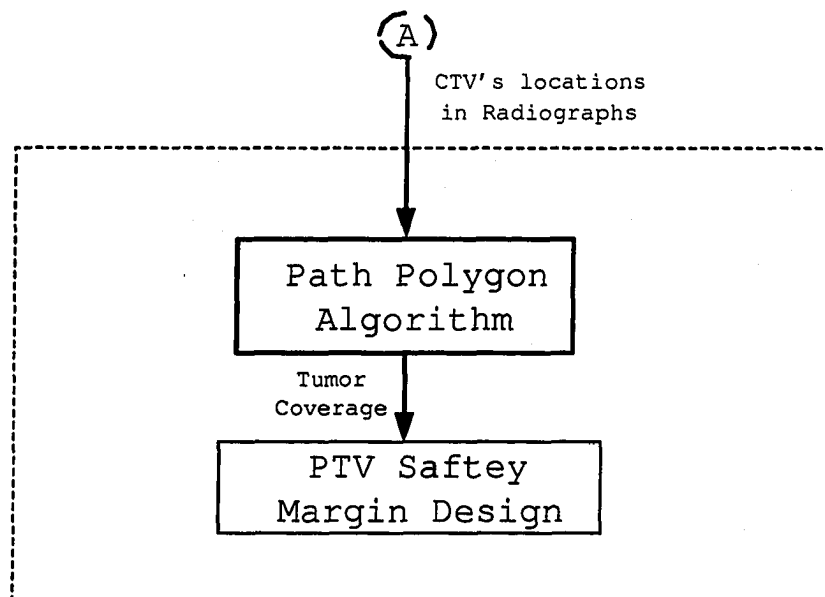


Figure 3.5: Tumor coverage computation.

the designed PTV and the computed tumor coverage, the PTV margins for each direction may be reduced to the tight tumor coverage provided that other physical uncertainties have no impact on the treatment.

### 3.4 Stage 3: Real Time Tumor Tracking

The tumor coverage computation may assist in reducing the margin added to the CTV during treatment planning. However, this solution can only benefit the non-critical cases, in which OARs keep enough distance to the tumor. For other cases with small, mobile tumors within or near critical structures, more advanced techniques such as gated irradiation or dynamically tracking are required to deliver the prescribed doses to the tumor and spare the nearby OARs. Despite which method issued, we need to obtain the real-time tumor positions during treatment. Most previous studies focus on using implanted markers [17, 42, 45, 46]. These invasive methods usually make patients feel uncomfortable and their clinical trials also showed that these methods are not suitable for some types of patients.

To provide a comfortable, practical way to deliver radiation to the moving tumor, a real time tumor tracking stage is presented in our solution. This stage uses the CTV information in radiographs and the correlated positions of external skin markers to monitor tumor motion dynamically.

Images taken with a high energy treatment machine lack detailed structures and require some image processing to enhance the visible features. Therefore, it is almost impossible to use them for monitoring purposes during treatment. However, it is observed that the skin nearby lungs, and breasts is also moving synchronously when patients are breathing. Based on this observation, it is possible to synchronize these X-ray radiographs with the external skin markers.

During simulation, before the fluoroscopic video is captured, a small plastic block with three infrared reflective markers is placed on the patient's skin surface near the tumor. When the resulting images are captured by the camera, the information

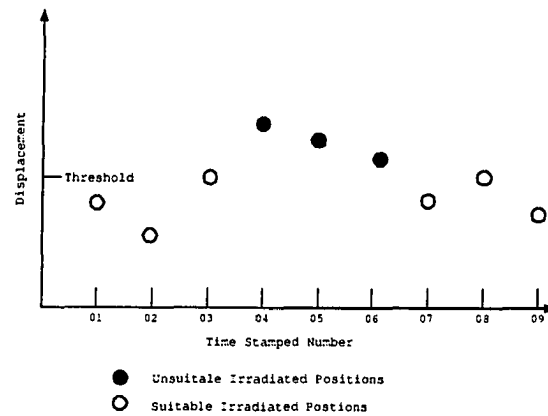


Figure 3.6: Displacement analysis of treatment fields

about the position of each marker can be digitized. That means each X-ray radiograph corresponds to a particular position of these skin markers. In the Ottawa Reginal Cancer Center, a Patient Position Monitoring (PPM) system was developed a few years ago [13]. This system is capable of measuring the Cartesian coordinates of small optical targets placed on the patient's skin surface during radiation therapy. When these markers move between measurements, the system determines the change in target position and reports this change. Research is still being done with the emphasis on the correlation study between external markers and the internal tumor motion caused by respiration. By synchronizing these X-ray radiographs with the Cartesian coordinates of the skin markers, we can get a tumor's position.

Through the displacement analysis between these tumor positions (represented by CTV contours) and the treatment fields, the gating knowledge about the skin markers can be obtained.

Instead of computing the tumor coverage, we analyze the geometric matching between the tumor region of each X-ray radiograph and its corresponding treatment field. By applying the threshold of tolerated displacement, these radiographs can be separated into two groups: suitable positions, in which the radiation can be turned

on, and unsuitable positions, in which the radiation should be turned off. As illustrated in Figure 3.6, all the X-ray radiographs with tumor displacements below the given threshold are marked as suitable and those above as unsuitable ones. If there are no critical organs around the tumor, slight displacement may be allowed without apparent damage to the patient. If any OAR is situated within a few millimeters from the tumor, maximum accuracy is required for use of high-dose irradiation. Usually, radiation oncologists can determine this threshold of the allowed maximal displacement during the treatment planning. However, in some cases where the tolerated value is very difficult to define, oncologists could be involved in making the decision of whether a position is suitable or not for irradiation. Since each radiograph corresponds to one particular position of the external skin markers, then we can obtain the gating information about these external skin markers. During treatment, the irradiation can be turned on or off based on this knowledge. For the example given in Figure 3.6, the time period with the external skin markers located in time stamps numbered 04, 05 and 06 are the “turn-off” period while 01, 02, 03, 07, 08 and 09 would be the “turn-on” period.

Figure 3.7 shows the processing steps in this real-time tumor tracking stage. During treatment planning, video files of the external skin markers are first captured and converted to computer-stored formats. Then, a third party tool is used to extract the individual images from the video files. These synchronized images are correlated with the CTV’s locations obtained from the previous stage. After this step, the correlation between the external skin markers and the tumor locations can be obtained and exported to treatment.

During treatment, one application of this correlation is to be used in the displacement analysis of gated radiation. another is to be used for adaptive radiation. Arguably, with the correlation between the coordinates of these external markers and the positions of the internal tumor, the beam can be adapted to follow the moving target or the couch of the patient can be adapted to align the moving target to follow the beam continuously. However, further discussion about this mobile delivery system is beyond our work here.

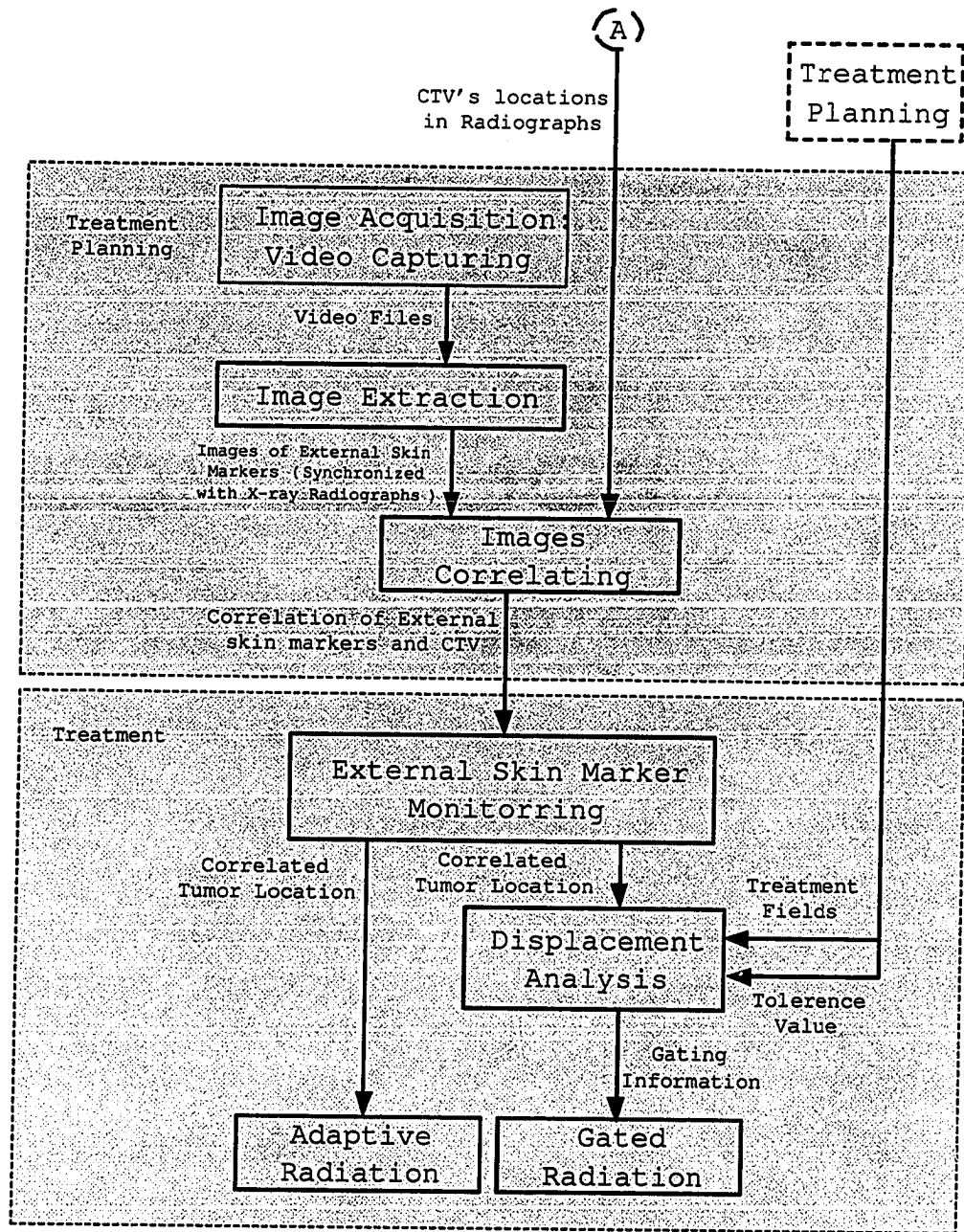


Figure 3.7: Real-time tumor tracking.

# Chapter 4

## Path Polygon Algorithm

In Chapter 3, we introduced a new solution to compensate for tumor motion caused by a patient's breathing. For this solution, one of the critical steps is how to compute a moving tumor's coverage. In this chapter, we present a path polygon algorithm which can compute the path of a moving object if it can be contoured as a simple polygon.

Section 4.1 explains how the tumor coverage problem can be transformed into this path polygon problem. Section 4.2 presents notation and definitions used in this algorithm description followed by the properties of a path polygon which we give in Section 4.3. In Section 4.4, we describe our algorithm and in Section 4.5, we summarize our results and discuss the future work related to this algorithm.

### 4.1 The Tumor Coverage Problem

The tumor coverage problem arises in radiation therapy when a tumor is located in a lung, a breast or an abdomen. Since the tumor moves due to the patient's breathing, the targeted area includes not only the tumor volume itself but also an additional safety margin around the tumor. In order to tighten this safety margin in each direction, we must know the potential tumor's region of movement during

radiation. We refer to this problem as the *tumor coverage problem*.

Similar problems also arise in computer graphics animation and in robotics. In computer animation, a trajectory is defined for a given object and the goal is to determine the intermediate locations between the start position and the end position (e.g., the motion of a hand)[10]. In robotics, a very similar problem arises in robot path planning. Here the objective is to find a path for a robot from a starting point  $s$  to a destination point  $d$  such that the robot does not collide with obstacles along the way. Algorithms which are based on Minkowski sums are used to compute the configuration space of the robot. Once computed, a search for a valid path through the configuration space between  $s$  and  $d$  is executed [2].

In our solution, we estimate the tumor coverage by computing its moving path before treatment. In general, a tumor can be outlined as a simple polygon on each radiograph. Assuming the tumor's shape does not change through out its movement, the tumor's movement can be represented by a continuous moving chain. The patient's breathing pattern allows us to separate this chain into different monotone chains (only moving along one direction such as up or down). Under this assumption, this tumor coverage problem becomes the following path polygon problem in geometry: Given an  $n$ -vertex simple polygon  $P = \{v_1, v_2, \dots, v_n\}$  whose vertices are given in counter clockwise (CCW) order, and a monotone chain  $C = \{c_1, c_2, \dots, c_m\}$ , compute the minimum area polygon  $Q$  that contains all the region covered by  $P$  as it is translated along the point of  $C$ . Here, we present a simple algorithm when  $P$  is a convex polygon.

## 4.2 Preliminaries

For simplicity, we assume that  $C$  is a strictly decreasing monotone chain in the  $y$  direction, namely,  $y(c_i) > y(c_{i+1}), 1 \leq i \leq m$ .

We denote by  $v_t$  the topmost vertex of  $P$  (i.e., the vertex  $v \in P$  with the largest  $y$ -coordinate) and similarly by  $v_b$  the bottommost vertex of  $P$  (see Figure 4.1(a)).

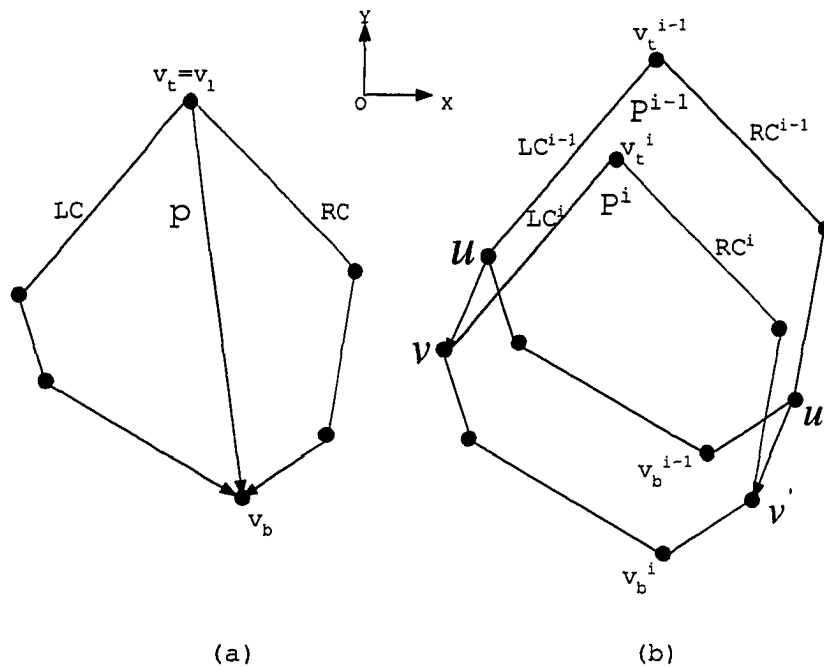


Figure 4.1: The notations used in the path polygon algorithm.

Without loss of generality, we assume that  $v_t = v_1$ . Since by assumption,  $P$  is convex, vertices  $v_t$  and  $v_b$  divide  $P$  into two monotone chains: **the left chain**, denoted as  $LC$  whose vertices, in CCW order, are  $\{v_1, v_2, \dots, v_b\}$ , and **the right chain**, denoted as  $RC$  whose vertices, in CCW order, are  $\{v_b, v_{b+1}, \dots, v_1\}$ .

In our problem, polygon  $P$  is translated along chain  $C$ . Denoted by  $P^i$  the copy of  $P$  when it is positioned at vertex  $c_i \in C$  and the vertices of  $P^i$  are  $\{v_1^i, v_2^i, \dots, v_n^i\}$ . The topmost vertex, bottommost vertex, left chain and right chain of  $P^i$  are denoted by  $v_t^i, v_b^i, LC^i$  and  $RC^i$ , respectively.

Vertices  $u \in P^{i-1}$  and  $v \in P^i$  are **extreme vertices**, if  $P^{i-1}$  and  $P^i$  lie in the same half plane defined by a line  $L$  through  $u$  and  $v$  (see Figure 4.1(b)). Vertices  $u$  and  $v$  are **left extreme vertices** if  $P^{i-1}$  and  $P^i$  lie on the right side of  $L$ . Similarly, vertices  $u$  and  $v$  are **right extreme vertices** if  $P^{i-1}$  and  $P^i$  lie on the left side of  $L$ . The segment  $\overline{uv}$  is termed **an extreme edge**.

The solution to our problem is the minimum area polygon (called the *path polygon*  $P^{i,k}$ ) ( $1 \leq i \leq k \leq m$ ), which includes the entire region touched by  $P$  as it is translated along chain sub chain  $c_i, \dots, c_k$  of  $C$ . The topmost and bottommost vertices of  $P^{i,k}$  are denoted as  $v_t^{i,k}$  and  $v_b^{i,k}$ , respectively. Similarly, the left chain and the right chain of  $P^{i,k}$  are denoted by  $LC^{i,k}$  and  $RC^{i,k}$ .

### 4.3 Properties of the Path Polygon

Recall, that in our problem,  $P$  is a convex polygon and, for simplicity,  $C$  is a strictly decreasing monotonic chain in the  $y$ -direction. Thus, we observe the following lemmas:

**Lemma 1.** *Given a convex polygon  $P$  and a monotonically decreasing chain  $C$  in the  $y$ -direction, the path polygon,  $P^{i,i+1}$ , which is a result of translating  $P$  along segment  $\overline{c_i c_{i+1}}$  of  $C$  is the convex hull  $Q$  of  $P^i$  and  $P^{i+1}$ .*

*Proof.* If  $P^{i,i+1} \cap Q = Q$  and  $P^{i,i+1} \cap Q = P^{i,i+1}$ , then we can conclude that  $P^{i,i+1} = Q$ , where  $Q$  denotes the convex hull of  $P^i$  and  $P^{i+1}$  (i.e.,  $Q = CH(P^i, P^{i+1})$ ). Now we assume that  $P^{i,i+1} \neq Q$ , then two cases arise:

**Case 1**  $P^{i,i+1} \cap Q \neq Q$ : in this case there is a point  $o \in Q$  but  $o \notin P^{i,i+1}$  (Figure 4.2 (a)). Let  $L$  be a line parallel to  $\overline{c_i c_{i+1}}$  through  $o$  and let  $v$  be the intersection between  $L$  and  $P^i$ . Let  $v'$  be a point on  $P^{i+1}$  such that when  $P^i$  is overlayed on  $P^{i+1}$  then  $v = v'$ . In this case  $P^{i,i+1}$  does not contain all the segment  $\overline{vv'}$  and therefore it cannot be a path polygon.

**Case 2**  $P^{i,i+1} \cap Q \neq P^{i,i+1}$ : in this case there exists a point  $o \in P^{i,i+1}$  but  $o \notin Q$  (Figure 4.2 (b)). Note, that  $o \notin P^i$  and  $o \notin P^{i+1}$  since  $o \notin Q$ . Let  $L$  be a line parallel to  $\overline{c_i c_{i+1}}$  through  $o$  and let  $v$  be the intersection of  $L$  and  $P^i$ . Let  $v'$  be a point on  $P^{i+1}$  such that when  $P^i$  is overlayed on  $P^{i+1}$  then  $v = v'$ . Since  $o \notin Q$  implies that line segment  $\overline{vv'} \notin Q$  contradicting the fact that  $Q = CH(P^i, P^{i+1})$ .

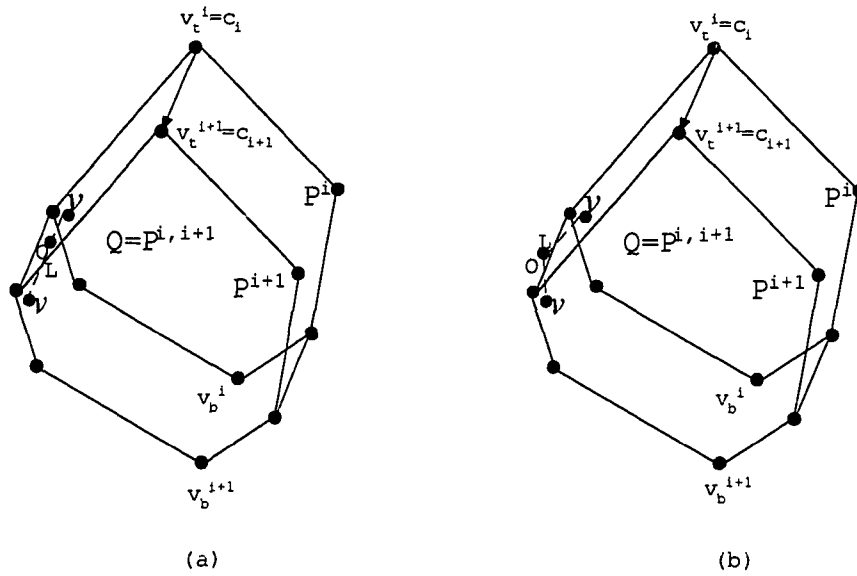


Figure 4.2: Two cases if  $P^{i,i+1} \neq CH(P^i, P^{i+1})$ .

□

The fact that  $P^{i,i+1}$  is convex leads to the following corollary regarding the number of vertices in  $P^{i,i+1}$ .

**Corollary 1.** *Given a convex polygon  $P = \{v_1, v_2, \dots, v_n\}$  and a monotonically decreasing chain  $C$  in the  $y$ -direction, the number of vertices of the path polygon,  $P^{i,i+1}$ , which is a result of translating  $P$  along segment  $\overline{c_i c_{i+1}}$  of  $C$ , is  $n + 2$ .*

The convexity of the path polygon may not hold when  $C$  consists of 3 or more vertices. In this case the path polygon is monotone (see lemma 3 below). Moreover, the top and bottom vertices of the resulting path polygon can be easily computed (see lemma 2).

**Lemma 2.** *Given a convex polygon  $P$  and a monotonically decreasing chain  $C$  in the  $y$ -direction, the topmost and bottommost vertices (i.e.,  $v_t^{i,i+k}$  and  $v_b^{i,i+k}$ ) of the path polygon  $P^{i,i+k}$  are  $v_t^i$  and  $v_b^{i+k}$ , respectively.*

*Proof.* Since  $v_t^i$  is the starting topmost vertex and the successive vertices decrease in the  $y$ -direction,  $v_t^{i,i+k}$  must necessarily be  $v_t^i$ . By using the similar argument for the bottom most vertex of  $P^{i,i+k}$ , we can conclude that  $v_b^{i,i+k}$  must be  $v_b^{i+k}$ .

□

**Lemma 3.** *Given a convex polygon  $P$  and a monotonically decreasing chain  $C$  in the  $y$ -direction, the path polygon  $P^{i,i+k}$  is  $y$ -monotone.*

*Proof.* By lemma 2,  $v_t^{i,i+k}$  and  $v_b^{i,i+k}$  divide  $P^{i,i+k}$  into two chains the  $LC^{i,i+k}$  and  $RC^{i,i+k}$ . If  $P^{i,i+k}$  is not  $y$ -monotone then either  $LC^{i,i+k}$  or  $RC^{i,i+k}$  are not  $y$ -monotone. Without loss of generality assume that  $LC^{i,i+k}$  is not  $y$ -monotone. Then there are three consecutive vertices  $u, v, w \in LC^{i,i+k}$  where the monotonicity of  $LC^{i,i+k}$  is violated for the first time. Namely, the segment  $\overline{vw}$  is added to such that  $y(u) > y(v)$  and  $y(w) > y(v)$  (see Figure 4.3). Assume that vertex  $v$  is a result of adding  $P^j$  to  $P^{i,j-1}$  and vertex  $w$  is a result of adding  $P^{j+1}$  to  $P^{i,j}$ . There are two cases to examine:

**Case 1  $w$  is to the left of  $\overline{vw}$  (Figure 4.3(a)):** in this case  $w = v_t^{j+1}$  and from lemma 2,  $v = v_b^j$ . Since  $C$  is a monotonically decreasing chain it implies that  $y(v_t^{j+1}) < y(v_t^j)$  and that  $y(v_b^{j+1}) < y(v_b^j)$ . Polygon  $P^j$  is to the right of  $\overline{vw}$  and therefore,  $\overline{vw} \in CH(P^j, P^{j+1})$ . This contradicts the assumption that  $\overline{vw} \in LC^{i,j+1}$ .

**Case 2  $w$  is to the right of  $\overline{vw}$  (Figure 4.3(b)):** in this case the interior of  $P^j$  and  $P^{j+1}$  are to the left of  $\overline{vw}$ . Since  $\overline{vw}$  has a positive slope it implies that  $y(v_b^{j+1}) > y(v_b^j)$ . This contradicts the monotonicity of  $C$ .

□

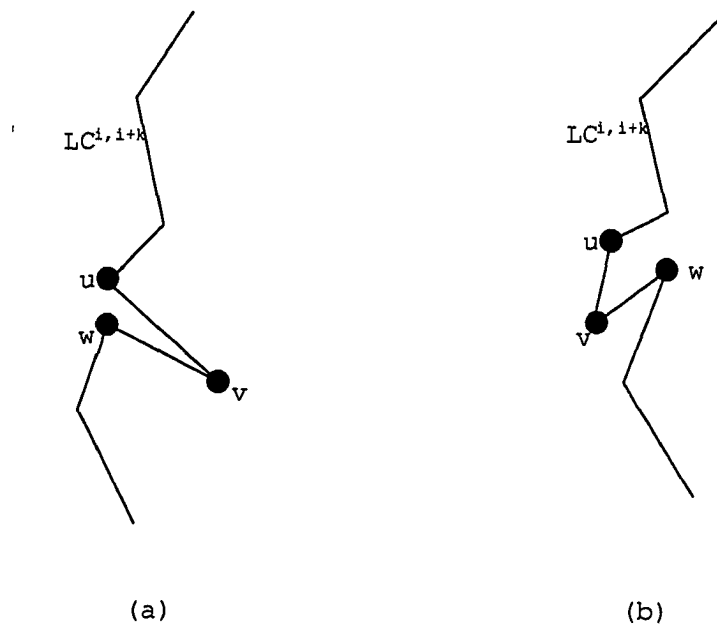


Figure 4.3: The two cases that the monotonicity of the  $LC^{i,i+k}$  can be violated.

## 4.4 Algorithm

In this section we describe our algorithm for finding the path polygon of a convex polygon. Our algorithm is based on the fact that  $P^{i,i+1}$  is convex (see lemma 1) and that  $P^{i,i+k}$  is monotone (see lemma 3). The idea behind the algorithm is as follows. Starting from  $c_1$ , make a copy of  $P$  and place it at  $c_i$  to form  $P^i$ . Then add  $P^i$  to  $P^{1,i-1}$  one at a time for all  $2 \leq i \leq k$ .

We first describe, in Section 4.4.1, how to add  $P^i$  to  $P^{1,i-1}$ , which is the crux of the algorithm. Then in Section 4.4.2 we present our algorithm and the time complexity.

### 4.4.1 Adding $P^i$ to $P^{1,i-1}$

In this section we only present the algorithmic steps of updating the left chain of  $P^{1,i-1}$ . Similar and symmetrical steps are taken to update the right chain of  $P^{1,i-1}$ .

**Observation 1.** Let  $\overline{uv}$  be the left extreme edge of  $CH(P^{i-1}, P^i)$  where  $u \in P^{i-1}$  and  $v \in P^i$ . When updating  $LC^{1,i-1}$  there are two cases to consider.

**Case 1** Vertex  $u \in LC^{1,i-1}$  (see Figure 4.4(a)). In this case vertices  $u, v, \dots, v_b^i$  replace vertices  $u, \dots, v_b^{1,i-1} \in LC^{1,i-1}$ .

**Case 2** Vertex  $u \in P^{1,i-1}$  ( $u \notin LC^{1,i-1}$ ) (see Figure 4.4(b)). In this case vertices  $w, v, \dots, v_b^i$  are used to update  $LC^{1,i-1}$ , where  $w$  is the intersection between  $LC^{1,i-1}$  and  $LC^{i-1,i}$ .

*Proof.* In Case 1, since  $u \in LC^{1,i-1}$  and  $\overline{uv}$  is the left extreme edge of  $CH(P^{i-1}, P^i)$ , therefore  $\overline{uv}$  is outside or partially outside  $LC^{1,i-1}$ . Thus, it must be added to  $LC^{1,i-1}$ . Then, the remaining vertices,  $v, \dots, v_b^i$ , are added as described in Lemma 1.

In Case 2, since  $u \notin LC^{1,i-1}$  but  $u \in P^{1,i-1}$ , therefore it cannot be part of  $LC^{1,i}$ . However,  $v_b^i$  must be a part of  $P^{1,i}$  and  $v_b^i \notin P^{1,i-1}$ . It implies that  $LC^{i-1,i}$  and  $LC^{1,i-1}$  must intersect. Once the intersection,  $w$ , of  $LC^{i-1,i}$  and  $LC^{1,i-1}$  is found, the intersection point is added to  $LC^{1,i-1}$  followed by vertices of  $v, \dots, v_b^i \in LC^{i-1,i}$  as a result of lemma 1.  $\square$

#### Algorithm AddPolygon

- {The function adds polygon  $P^i$  to path polygon  $P^{1,i-1}$ }
- {Updating the left chain of  $P^{1,i-1}$ }
- 1: find the convex hull of  $P^{i-1}, P^i$
- 2:  $u \leftarrow$  left extreme vertex of  $P^{i-1}$
- 3:  $v \leftarrow$  left extreme vertex of  $P^i$
- 4: **if**  $u \in LC^{1,i-1}$  **then** {see Figure 4.4(a)}
- 5:   remove vertices  $u, \dots, v_b^{1,i-1}$  from  $LC^{1,i-1}$
- 6:    $LC^{1,i} \leftarrow LC^{1,i-1} \cup u, v, \dots, v_b^i$
- 7: **else** {here  $u \notin LC^{1,i-1}$ , thus,  $LC^{i-1,i} \cap LC^{1,i-1}$  may intersect at a new vertex (see Figure 4.4(b))}
- 8:   find edges  $\overline{uv} \in P^{i-1,i}$  and  $\overline{u'v'} \in P^{1,i-1}$  such that  $\overline{uv} \cap \overline{u'v'} \neq \emptyset$
- 9:    $w \leftarrow \overline{uv} \cap \overline{u'v'} \neq \emptyset$

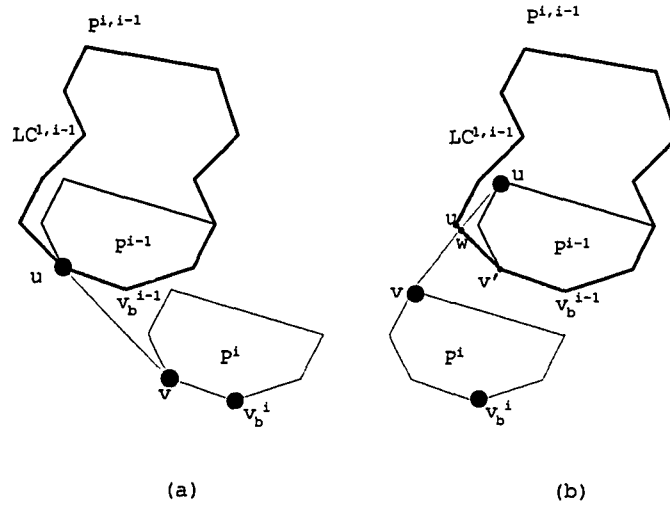


Figure 4.4: The two cases for adding polygon  $P^i$  to  $P^{1,i-1}$ : a. extreme vertex  $u \in LC^{1,i-1}$  and b. extreme vertex  $u \notin LC^{1,i-1}$

10: remove vertices  $v', \dots, v_b^{1,i-1}$  from  $LC^{1,i-1}$

11:  $LC^{1,i} \leftarrow LC^{1,i-1} \cup w, v, \dots, v_b^i$

12: end if

{Update the right chain of  $P^{1,i-1}$ }

{This case is similar to updating the left chain and therefore omitted}

**endalgorithm**

Next we prove the correctness of the algorithm. First we show that if  $u \notin LC^{1,i-1}$  then  $LC^{1,i-1} \cap LC^{i-1,i}$  at a single vertex.

**Lemma 4.** *Given a convex polygon  $P$  and a monotonically decreasing chain  $C$  in the  $y$ -direction, if  $u \notin LC^{1,i-1}$ , where  $u$  is the left extreme edge of  $P^{i-1}$  then  $LC^{1,i-1}$  intersects the  $LC^{i-1,i}$  only once.*

*Proof.* The proof is given by contradiction. Assume that  $LC^{1,i-1}$  and  $LC^{i-1,i}$  intersect more than once. Let edges  $\overline{st}$  and  $\overline{qr}$  be the edges that  $\overline{vu}$  intersects  $LC^{1,i-1}$  for the first time (enters  $P^{1,i-1}$ ) and for the second time (leaves  $P^{1,i-1}$ ), respectively (see



for uniting  $LC^{i-1,i}$  and  $LC^{1,i-1}$ . First option occurs when  $u \in LC^{1,i-1}$  where  $u$  is that the left extreme edge of  $P^{i-1}$ . Here,  $LC^{1,i}$  is monotone because the subchain of  $LC^{1,i-1}$  consisting of  $\{v_t^{1,i-1}, \dots, u\}$  is monotone and the concatenated subchain of  $LC^{i-1,i}$  consisting of  $\{u, \dots, v_b^{i-1,i}\}$  is monotone. This case is handled in lines 5, 6 of function AddPolygon.

The second option is that  $u \notin LC^{1,i-1}$  where  $u$  is the left extreme edge of  $P^{i-1}$ . Here, by lemma 4 there is an intersection point  $w$  such that the subchain of  $LC^{1,i-1}$  consisting of  $\{v_t^{1,i-1}, \dots, w\}$  is monotone and the concatenated subchain of  $LC^{i-1,i}$  consisting of  $\{w, \dots, v_b^{i-1,i}\}$  is monotone. This case is handled in lines 8 – 11 of function AddPolygon.

**Case (b) The path polygon is the minimum size polygon containing  $P$  :** The input polygon  $P^{1,i-1}$  is a path polygon and therefore the minimum size polygon that covers the regions occupied by  $P$  as it is translated along subchain  $\overline{c_1, c_2, \dots, c_{i-1}}$ . From lemma 1,  $P^{i-1,i}$  is a path polygon and therefore the minimum size polygon that covers the regions occupied by  $P$  as it is translated along  $\overline{c_{i-1}c_i}$ . Therefore the union of the two path polygons is the minimum size polygon that covers the regions occupied by  $P$  as it is translated along subchain  $c_1, \dots, c_{i-1}$ . Function AddPolygon finds the union of the two polygons by determining the left and right chains of the output polygon.

□

During its execution the function AddPolygon adds new vertices to the output path polygon  $P^{1,i}$ . However, the function also removes vertices from the polygon. Although, the total number of vertices that can be added is  $O(n)$  by Corollary 1 the number of vertices in  $P^{i-1,i}$  grows by constant number. Recall that the function removes the same number of vertices. Thus, we obtain the following corollary.

**Corollary 2.** *The maximum number of vertices in path polygon  $P^{1,m}$  is  $n + 2m$ .*

The time complexity of the function is given next.

**Lemma 6.** *Function AddPolygon requires  $O(\log n \log(n + i) + n)$  time in the worst case to add polygon  $P^i$  to  $P^{1,i-1}$ , where  $n$  is the number of vertices in  $P^i$ .*

*Proof.* Finding the  $CH(P^{i-1}, P^i)$  can be done in  $O(\log n)$  time (note that  $P^{i-1}$  and  $P^i$  are two copies of the same polygon and the supporting lines are parallel to  $\overline{c_{i-1}c_i}$ ). Finding the intersection between  $LC^{i-1,i}$  and  $LC^{1,i-1}$  can be done in  $O(\log n \log l)$  time, which is similar to merging two convex hulls [30], where  $l$  is the number of vertices in  $P^{1,i-1}$ . By Corollary 2, the number of vertices in  $P^{1,i-1}$  is bounded by  $n + 2i$  which yields a time complexity of  $O(\log n \log(n + i))$ . Lastly, the function adds new vertices to  $LC^{1,i-1}$  and  $RC^{1,i-1}$ . In the worst case, all the vertices of  $P^i$  must be added to  $LC^{1,i-1}$  and  $RC^{1,i-1}$ , which is linear. □

In this section we showed how a single polygon is added to an existing path polygon. Next we present the algorithm that computes the complete path polygon.

#### 4.4.2 Main Algorithm

In this section we present the main algorithm which computes the complete path polygon  $P^{1,m}$ .

**Algorithm** ComputePathPolygon( $C, P, PP$ )

{ $C = \{c_1, c_2, \dots, c_m\}$  is a monotone chain in the y-direction}

{ $P$  is the input convex polygon}

{ $PP$  is the output path polygon}

1:  $P^{1,1} \leftarrow P^1$ ;

2: **for**  $i \leftarrow 2$  to  $m$  **do**

3:   compute polygon  $P^i$

4:   AddPolygon( $P^{1,i-1}, P^i$ )

5: **end for**

6:  $PP \leftarrow P^{1,m}$

**endalgorithm**

Next we show that the algorithm finds the path polygon  $P^{1,m}$  and discuss its time complexity.

**Lemma 7.** *Given a convex polygon  $P = \{v_1, v_2, \dots, v_n\}$  and a monotonically decreasing chain  $C = \{c_1, c_2, \dots, c_m\}$  in the  $y$ -direction, the function `ComputePathPolygon` correctly computes the path polygon  $P^{1,m}$ .*

*Proof.* We give here a proof by induction on the size of the monotone chain  $C$ . The base case is when  $C$  consists of one vertex. In this case the function `ComputePathPolygon` returns  $P^1$ . Assume that function `ComputePathPolygon` correctly computes the path polygon  $P^{1,k}$  for a monotone chain  $C$  with  $k$  vertices. We must show that it correctly computes the path polygon for a monotone chain  $C$  with  $k + 1$  vertices. At iteration  $k + 1$ , the function invokes `AddPolygon` with the path polygon  $P^{1,k}$  and  $P^{k+1}$ . From the induction hypothesis polygon  $P^{1,k}$  was correctly computed by `ComputePathPolygon`. By lemma 5 the function `AddPolygon` correctly adds polygon  $P^{k+1}$  to  $P^{1,k}$  to form  $P^{1,k+1}$ .  $\square$

**Lemma 8.** *Given a convex polygon  $P = \{v_1, v_2, \dots, v_n\}$  and a monotonically decreasing chain  $C = \{c_1, c_2, \dots, c_m\}$  in the  $y$ -direction, the function `ComputePathPolygon` computes the path polygon  $P^{1,m}$  in  $O(mn + m \log n \log(n + m))$  time.*

*Proof.* The function `ComputePathPolygon` adds  $m - 1$  polygons to an initial path polygon  $P^{1,1}$ . At each iteration the algorithm computes the next  $P^i$  at a cost  $O(n)$ . The function also invokes the function `AddPolygon`  $m - 1$  times at a cost of  $O(\log n \log l_i + n)$  time where  $l$  is the size of path polygon  $P^{1,i}$ . However, by Corollary 2, the number of vertices in  $P^{1,i}$ ,  $1 \leq i \leq m$  is bounded by  $n + 2i$ . Thus, the cost of invoking `AddPolygon` is bounded by  $O(\log n \log(n + 2i) + n)$ . Therefore function `ComputePathPolygon` can compute the path polygon  $P^{1,m}$  in complexity  $O(mn + m \log n \log(n + m))$  time. This complexity becomes  $O(mn + m \log^2 n)$  if  $m = O(n)$ .  $\square$

## 4.5 Summary

In this chapter, we presented a solution for computing the area covered by a tumor as it moves during treatment. Our solution takes  $O(mn + m \log n \log(n + m))$  time where  $n$  is the number of vertices in the moving polygon and  $m$  is the number of vertices in the moving chain. We are currently working on pre-clinical tests to evaluate the efficiency and effectiveness of this algorithm. We are trying to incorporate our techniques into the radiation treatment cycle. We also plan to work on a 3D version of this problem to benefit the clinical system and other applications.

# Chapter 5

## System Implementation

Based on the solution introduced in Chapter 3 and the algorithm, which was presented in Chapter 4, we developed a software system that takes CT images, treatment plan information, and fluoroscopic video files as input data and outputs a polygon as the contour of tumor coverage. The output in our system is used as a guide for designing a PTV safety margin. The system is written in C++ using Visual C++ 6.0/MFC and implemented under Windows XP. In this chapter, we describe the functions of this system and explain how it works through a clinical example of system usage.

### 5.1 Overview

Our system input includes two types of data: (i) treatment plan data from the treatment planning system, which is stored as **DICOM** (Digital Imaging and Communications in Medicine) format files; and (ii) X-ray video which is taken during treatment simulation.

*DICOM* file format is commonly used in hospitals today. The DICOM 3.0 standards define information both for images and the data of patients, studies, reports, and other data groupings [33, 38]. In this system, we used three types of DICOM files. *DICOM CT* (Computed Tomograph) files store both the studying information

and the image data of CT slices, which are the cross sections of a patient's body and are obtained during the planning stage. *DICOM RT* (Radiation Therapy) structure file describes the information about the related structures of this patient's body such as GTV, CTV, PTV, bone structure, etc. With the exception of the above two types of information, the planning information about the radiation delivery, such as beam fields and fractions, is included in the DICOM RT plan file.

Video files are taken by a camera and are stored in the *.avi* format. In our system, these files are extracted as *.bmp* image files (referred to as X-ray radiographs) by third party software called *VirtualDub* [49], which is a free software and mainly geared toward processing AVI files.

The data flow of our system is illustrated in Figure 5.1. The data is presented by ellipses and the processes by rounded rectangles. The basic functions of this system are as follows:

1. Read treatment planning information from DICOM CT and RT files.
2. Reconstruct DRR images from CTs for the purpose of image registration.
3. Register tumor information from DRR images to X-ray radiographs included in video files.
4. Compute the tumor coverage of the moving tumor registered in X-ray radiographs.

All of these functions can be visualized and controlled using a graphical user interface.

The clinical test data which we used, included a total of 62 CT slices of information, a structure file, an RT plan file and three fluoroscopic video files. The video files were taken from different positions, as defined in treatment planning, and at the frequency of 10 frames per second. The video files consisted 60 – 180 films (6 – 18 seconds) and included several breathing cycles. As input to this system, the included frames were extracted with third party software and saved as bitmap images.

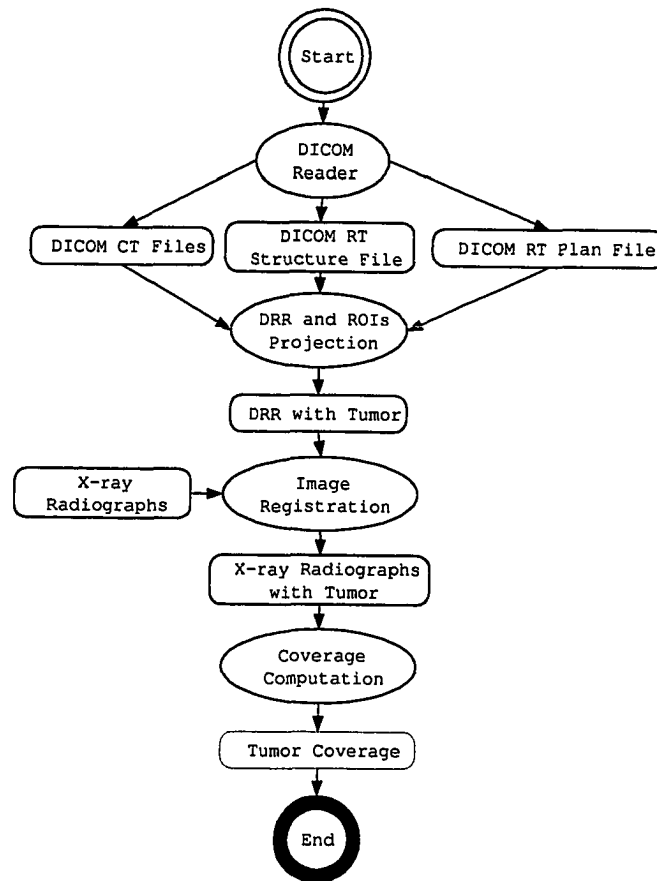


Figure 5.1: System data flow chart.

Before we start to describe this software system in detail, there is one thing we need to consider first. In this system, different coordinate systems are used and the transformation among them will be explained in Section 5.2. After that, each function of this system and its clinical example will be described.

## 5.2 Coordinate Systems

Since our input data uses different coordinate systems to describe its different information, a transformation is necessary to carry out further computations in our system.

DICOM 3.0 describes all the data under a coordinate system fixed to the patient, which is the patient-based coordinate system. In this coordinate system, the direction of the axes is defined fully by the patient's orientation. The  $x$ -axis is increasing to the left hand side of the patient. The  $y$ -axis is increasing to the posterior side of the patient. The  $z$ -axis is increasing toward the head of the patient. The origin can be defined at any point inside of the patient's body. Figure 5.2 illustrates a patient-based coordinate system when a patient is placed at Feet First, Supine (**FFS**) position.

However, the X-ray radiograph taken in the simulation room is described in an equipment-based coordinate system. This coordinate system is fixed in relation to the gantry equipment and the origin is always located in the ISO center, which is usually the mass center of target volume, and is defined in the patient-based coordinate system. Assuming the orientation of the patient is FFS position, then the  $y$ -axis of the equipment-based system is the same as the  $z$ -axis of the patient-based system. The  $z$ -axis is increasing to the project source from the ISO center. The  $x$ -axis is derived from  $y$ - and  $z$ -axes based on the rules of the right-hand system. The X-ray radiograph included in video files is an  $x$ - $y$  plane located with the fixed  $z$  value. Figure 5.3 shows an equipment-based coordinate system when a patient is placed at FFS position and the gantry angle is  $45^\circ$ . The illustrated portal image is the  $x$ - $y$  plane we discussed above.

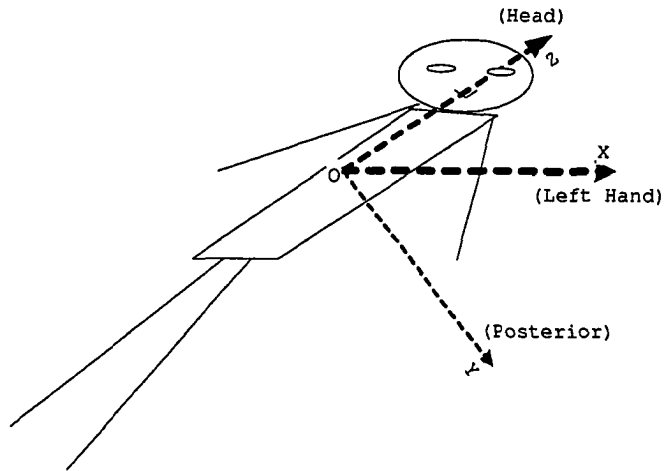


Figure 5.2: Patient-based coordinate system (FFS: Feet First, Supine position).

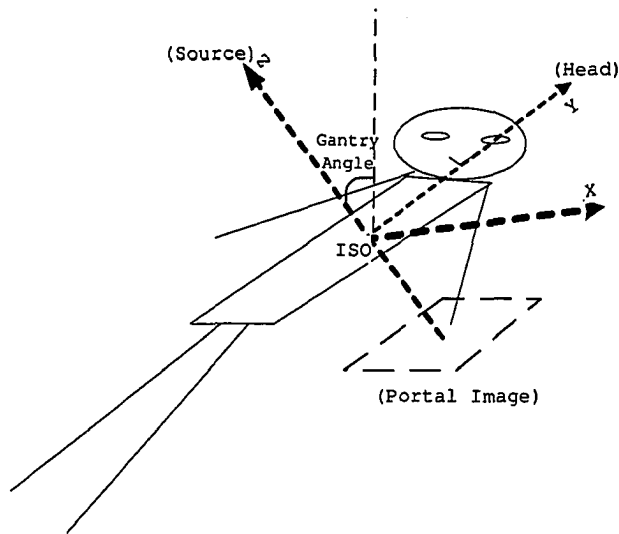


Figure 5.3: The Equipment-based coordinate system (The gantry orientation of the equipment is at  $45^\circ$  and the patient is positioned at FFS: Feet First, Supine position).

The information described in the patient system can be translated into the equipment system by the following two steps:

Step 1: Translation

$$\begin{aligned} X_{temp} &= X_{patient} - X_{iso}; \\ Y_{temp} &= Z_{patient} - Z_{iso}; \\ Z_{temp} &= -(Y_{patient} - Y_{iso}); \end{aligned} \tag{5.1}$$

Step 2: Rotation (Suppose the gantry angle is  $\Theta$ )

$$\begin{aligned} X_{room} &= X_{temp} \cos \Theta + Z_{temp} \sin \Theta; \\ Y_{room} &= Y_{temp}; \\ Z_{room} &= -X_{temp} + Z_{temp} \cos \Theta; \end{aligned} \tag{5.2}$$

Similarly, the information described in the equipment system can be translated into the patient system with the opposite transformation.

All of the data, including the output, is visualized in a screen-coordinate system. This coordinate system regards the left-top corner of the screen as the origin. X-axis points to the right and y-axis points to the bottom.

### 5.3 CT Images and Information Display

A single DICOM file consists patient treatment and image data. The patient treatment data (see the example listed in Appendix A) contains information about the patient's name, the type of scan, image dimensions, etc. Each item is identified with a unique pair of group number and element number (the first two numbers of each line). The image data stores a CT number for each pixel.

To convert these CT numbers into 255 grey scales, the terms of *Window Width* and *Window Center* are used in medical images as a simple way of describing the

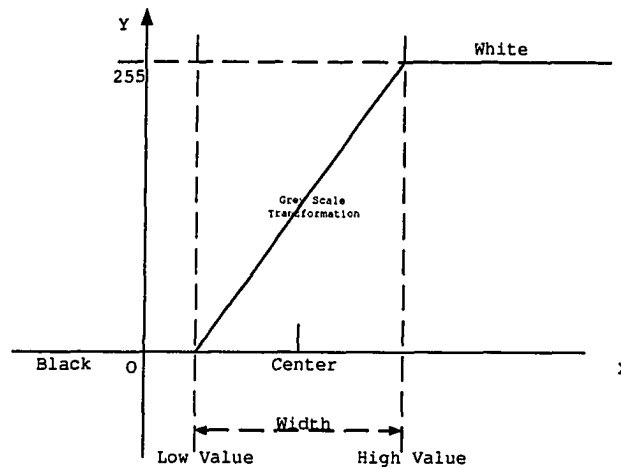


Figure 5.4: Grey scale transformation for CT images.

'brightness' and 'contrast'. Illustrated in Figure 5.4, *Window Width* is the range of CT numbers between its *Low Value* (all the CT numbers below this value are interpreted as black) and *High Value* (all the CT numbers above this value are interpreted as white). For the pixels with their CT numbers within this range, the following formula is used for its grey scale transformation.

$$\left[ \text{GreyScale} = \frac{\text{CTnumber} - \text{LowValue}}{\text{WindowWidth}} \times 255 \right] \quad (5.3)$$

*Window Center* is the middle CT number between the *Low Value* and the *High Value* ( $(\text{HighValue} + \text{LowValue})/2$ ). The default values of this C:W pair (*Window Center* and *Window Width*) are usually stored in DICOM CT description data identified as (0028,1050) and (0028, 1051). If not, minimal and maximum CT numbers are used to compute this C:W pair. The values of this pair are very important in generating a CT image (e.g., 400:2000 might be good for bone, while 50:350 might be a better choice for soft tissue).



Figure 5.5: CT slice and its information.

Our system displays CT slices with adjustable *Window Center* and *Window Width*. These displayed images can also be saved as .BMP images. All other non-image information in DICOM files can be dumped into a separated window. Figure 5.5 shows the 24th slice and its information. The information (see Appendix A in detail) describes that the resolution of this slice is  $512 \times 512$  and its left corner is located at  $(-275, -275, 20)$ . With the  $z$ -axis value of each slice, the thickness of the neighboring slices could be computed. The pixel spacing of this slice's row and column are 1.074219. All the values are measured in millimeters.

In the DICOM RT structure file, the information about the related structure of this patient's body is described as many Regions Of Interest (ROIs). These ROIs can be marked in CT images based on its contour information described in the RT file and slice position described in the CT file.

Appendix B shows part of the data dumped from a RT structure file, which describes the structure information for the above slices. Each ROI's data includes

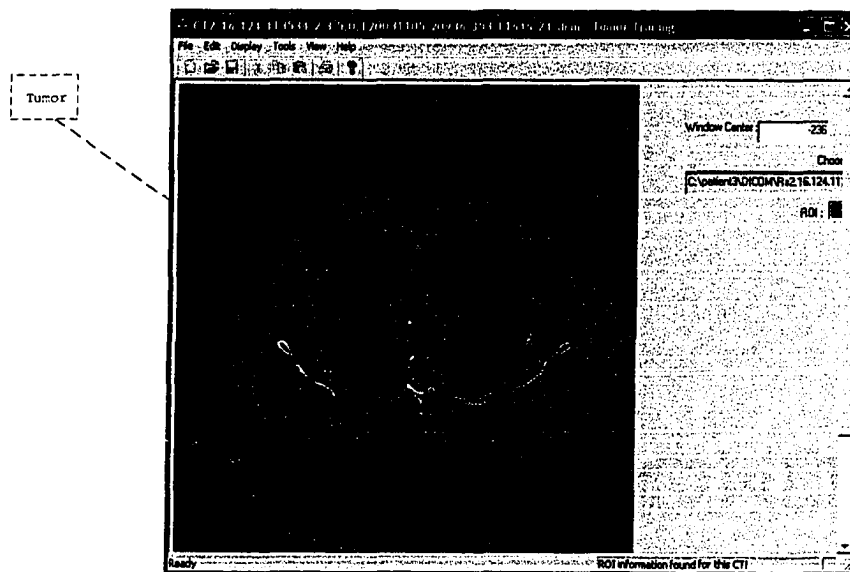


Figure 5.6: CT slice and marked target.

the slices involved and the closed plana formed by the points in each slice. In this data, we know that the tumor is described as ‘Target’ and its volume is located through slice 21 to 26. Figure 5.6 shows slice 24 with a marked in the right lung.

The DICOM RT plan file describes the detailed parameters for each beam such as the ISO position, gantry angle, MLC leaves position, source to ISO distance, etc. Appendix C lists part of the data dumped from the RT Plan file in our experimental data set. Figure 5.7 illustrates its three-beams treatment planning described in this file. The patient is placed at FFS position and the ISO center is defined at  $(-91.60, -13.90, 22.50)$ . The distance from the X-ray source to the ISO center is 1000 mm. Three beam fields are designed at Left Anterior Oblique (**LAO**), Left Posterior Oblique(**LPO**) and Right To Left Anterior (**RTLAT**) positions, respectively. LAO field is designed with the gantry angle of  $20^\circ$  and the collimator angle of  $0^\circ$ . Its MLC leaves position is defined with the width of  $(-38, 0, 40.0)$  and the height of  $(-35.0, 35.0)$ . LPO field is designed with the gantry angle of  $155^\circ$  and the collimator angle of  $0^\circ$ . Its MLC leaves position is defined with the width of  $(-40, 0, 43.0)$  and

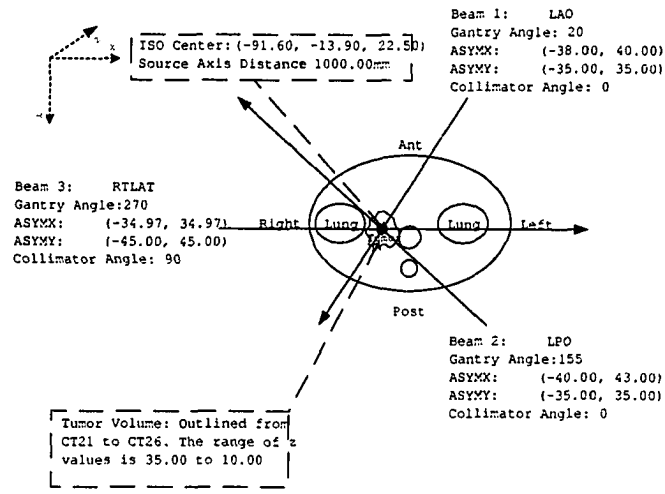


Figure 5.7: Beam fields using patient-based coordinate system.

the height of  $(-35.0, 35.0)$ . The RTLAT field is designed with the gantry angle of  $270^\circ$  and the collimator angle of  $90^\circ$ . Its MLC leaves position is defined with the width of  $(-34, 97, 34.97)$  and the height of  $(-45.0, 45.0)$ .

## 5.4 DRR and Image Registration

Based on the CT data in the DICOM CT files and the structure data in the DICOM RT file, our system generates a DRR image. Since all the data from DICOM files are defined under the patient-based coordinate system, the transformation discussed in Section 5.2 is used first to convert the data to the equipment-based coordinate system. The ISO center becomes the origin of the new coordinate system. Thus, the tumor volume, the patient's body and the reconstructed DRR can be described under the same coordinate system.

Figure 5.8 shows the configuration of a DRR and an example of the reconstructed

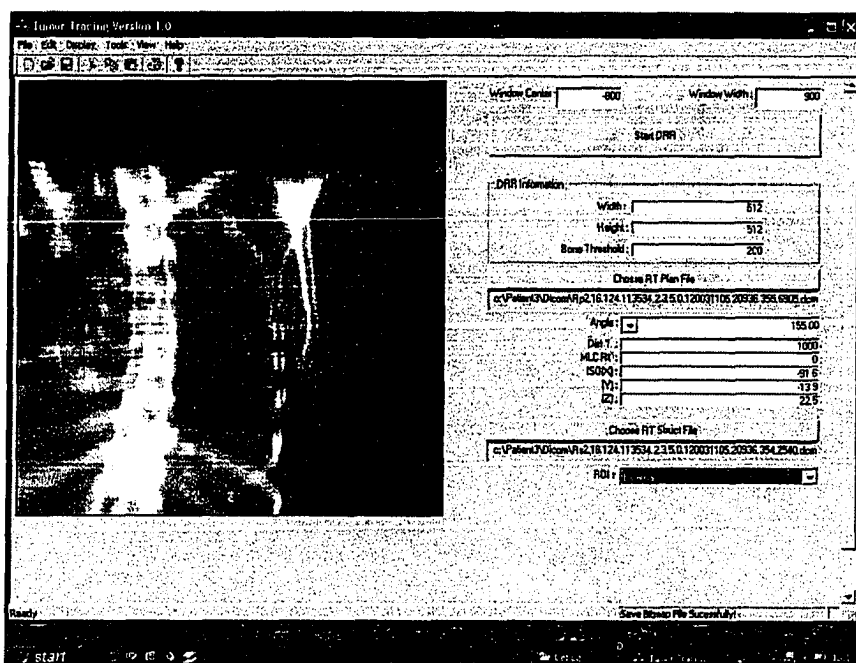


Figure 5.8: Digital reconstructed radiograph.

DRR in the LPO (Left Posterior Oblique) position. The user provides as input the following data: (i) the size of the DRR (the default value is  $512 \times 512$ ), (ii) the bone threshold for enhancing the bone structure (the default value is 200), (iii) the RT structure file which describes the information of the CT files and the ROI contour information for each slice. The system then reconstructs a digital radiograph from the given information (projected angle, distance, and ISO position) using the DRR algorithm described in Chapter 2. Depending on the ROI region, the system reads the related CT information, forms these CTs into a 3D model, and reconstructs the DRR.

The tumor information is also read from the DICOM RT structure file for each CT slice. The system uses a ray tracing method to project all the points of the tumor contour into the DRR plane from the radiation source. Under the equipment-based coordinate system, the radiation source  $o$  can be described as  $(0, 0, \text{SourceToISO})$ . The ray for each point  $p$  of the tumor contour is the vector pointing along a line from the radiation source to this point (i.e.  $\overline{op}$ ). Once the program has generated the ray of  $\overline{op}$ , the intersected point between  $\overline{op}$  and the DRR plane can be obtained using parametric lines. The intersected points with the DRR plane form the contour of the projected tumor.

To better register the tumor information onto the X-ray radiographs included in fluoroscopic video file, this system chooses the same parameters as used for the beam fields to reconstruct the DRR. As the configuration of Figure 5.8 shows, if we choose to read parameters from the DICOM RT plan file, then the system lists all the beam fields described in that file. The same position as the video file being taken can be selected from the list to reconstruct a DRR image.

The algorithm used here for image registration is a geometry-based algorithm with image landmark points on anatomy surface (see Chapter 2). First, the same orientation of the DRR and X-ray images should be loaded into the system. Then, three anatomic points need to be marked in both images (red in left and yellow in right). Based on the three points' coordinates in these two images, the system calculates a transformation from one image space to another image space. This

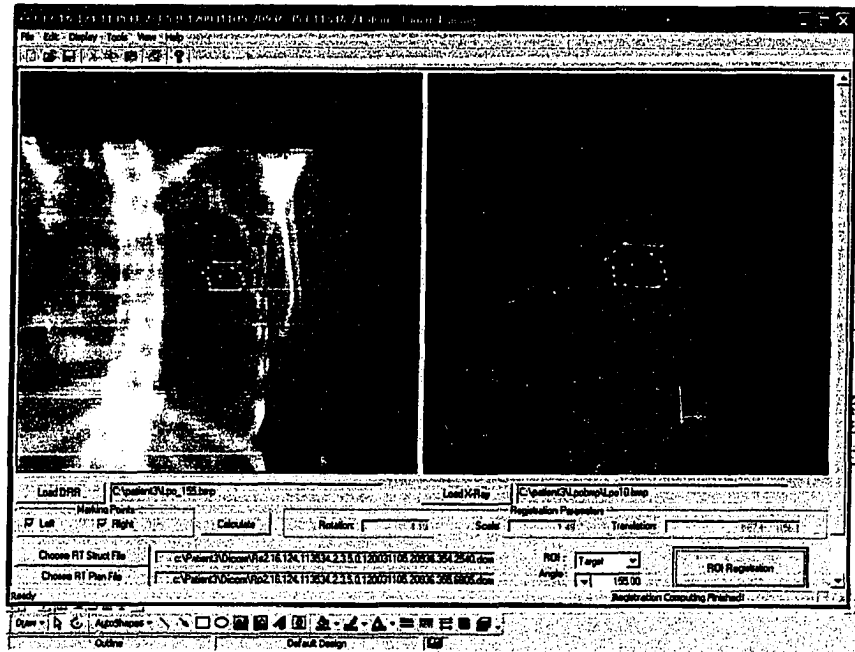


Figure 5.9: Image registration between DRR and X-ray images.

transformation includes the required rotation, scaling and translation. Therefore, tumor information read from the DICOM RT structure file can first be projected into the DRR plane using the same position parameters and then be registered in the X-ray radiograph with the computed transformation.

Figure 5.9 illustrates the image registration in our system. ‘LoadDRR’ loads the reconstructed DRR to the left source image while ‘LoadXRray’ loads the corresponding X-ray radiograph to the right target image. Then, the required landmarks can be drawn in the source or target image by checking ‘Left’ or ‘Right’ of ‘Marking Point’. Additional, to get the position parameters, the taken angle of these two images needs to be selected from the list of the RT plan file and the registered object needs to be selected from the ROIs of the RT structure file. In this example, the registered tumor is showed as a yellow polygon in the target image.

## 5.5 Tumor Coverage Computation

Once the tumor position is found in one X-ray radiograph, the system stores the tumor's shape as a simple polygon. The tumor's location in other radiographs of the same video file can be traced automatically or manually. The automatic method is based on a region's density to determine its likelihood of being a tumor. By moving the tumor shape around its previous location and comparing its interior density to the previous one, the region with the closest density can be obtained and treated as the tumor location. Alternatively, the user may manually move the tumor shape around and determine its best possible location.

Once the tumor information in all radiographs is obtained, these radiographs can be overlaid together in the order of their time stamps and the tumor's movement can be shown as a series of ordered simple polygons. Since all these polygons can be viewed as copies in different spatial positions, the system only stores the different positions of one vertex to represent these polygons' positions. The chain of the stored points (each one represents a polygon position) forms the trajectory of the first polygon's movement. Due to the respiratory pattern, this chain could increase or decrease along  $y$  direction. Based on the above data, our system computes the tumor coverage of these radiographs by using the following function.

**Algorithm** *ComputeTumorCoverage*(*MovementChain*, *FirstPolygon*, *TumorCoverage*)

- 1: initialize *TumorCoverage* as  $\emptyset$
- 2: obtain the counterclockwise convex hull from *FirstPolygon* and store it as *OriginPolygon*
- 3: store the moving direction of the first two points of *MovementChain* along  $y$  direction as *PreviousDirection*
- 4: set *StartPoint* as 1
- 5: **for**  $i \leftarrow 2$  to the number of vertices of *MovementChain* **do**
- 6:   determine the current moving direction of vertex  $i-1$  to vertex  $i$  of *MovementChain* along  $y$  direction and store it as *CurrentDirection*
- 7:   **if** *CurrentDirection* is different from *PreviousDirection* **then**
- 8:     set *EndPoint* as  $i - 1$

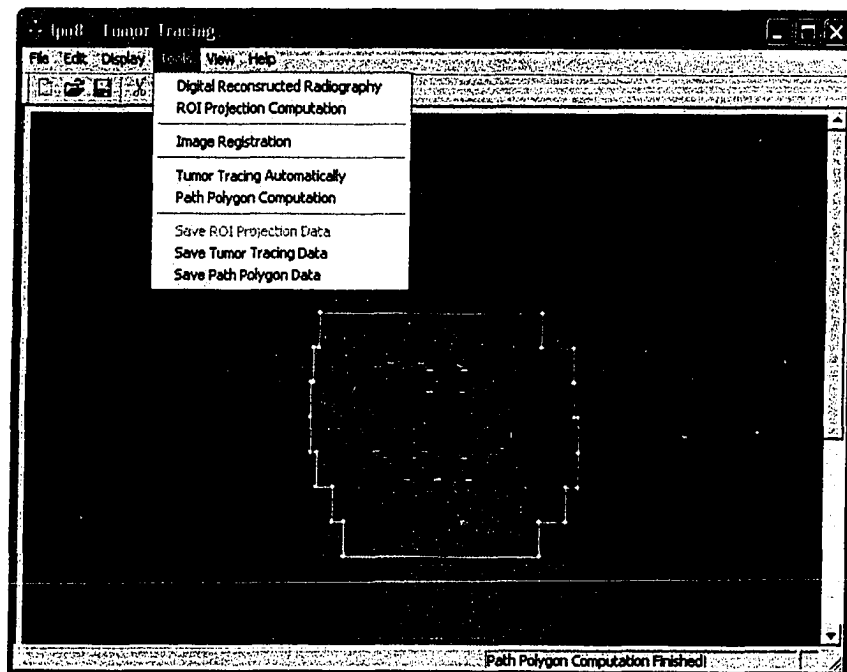


Figure 5.10: Tumor movement and its coverage.

```

{ComputePathPolygon is described in Chapter 4}
9:   ComputePathPolygon(sub chain between StartPoint and EndPoint of MovementChain,
    OriginPolygon, PathPolygon)
10:  set TumorCoverage = Union(TumorCoverage, PathPolygon)
11:  set PreviousDirection = CurrentDirection
12:  obtain the polygon in  $i - 1$  position from OriginPolygon and set it as
    OriginPolygon
13:  set StartPoint = EndPoint
14:  end if
15:  end for
endalgorithm

```

To use the tumor coverage tool, one radiograph needs to be loaded into the system first. Then, the system provides two methods to get the tumor shape: one is

from DRR reconstruction automatically and another is by drawing manually in the radiograph. After obtaining the tumor shape, the user can choose “Tumor Tracing Automatically” under the menu of “Tools” or load another radiograph to trace tumor manually. Figure 5.10 shows the detected tumors in four images and their computed coverage. The tumor’s contour for the current image is marked as red and the contour of its coverage is marked as blue. The yellow polygon is the original leaf positions to deliver the beam. We can see from this picture that the beam field is far bigger than needed. Our motivation is to output this tumor coverage and to use it for the purpose of optimizing the designed beam field at this particular position.

## 5.6 DRR Testing

We introduced the software tool and one clinical test in the previous sections. In this section, we show another two sets of patient data and the reconstructed DRRs.

One set of patient data includes 74 CT slices and 1 treatment field. Tumor appears from slice 30 to 32 and the treatment beam is from anterior to posterior. Figure 5.11 shows CT slice 32 and the reconstructed DRR with the tumor shape marked in yellow.

Another set of patient data includes 59 CT slices and 1 treatment beam from anterior to posterior position. Tumor appears from slice 11 to 29. Figure 5.12 shows CT slice 18 and the reconstructed DRR with the tumor shape marked in yellow.

The treatment data was missing from the X-ray which prohibited testing the tumor motion coverage computation.

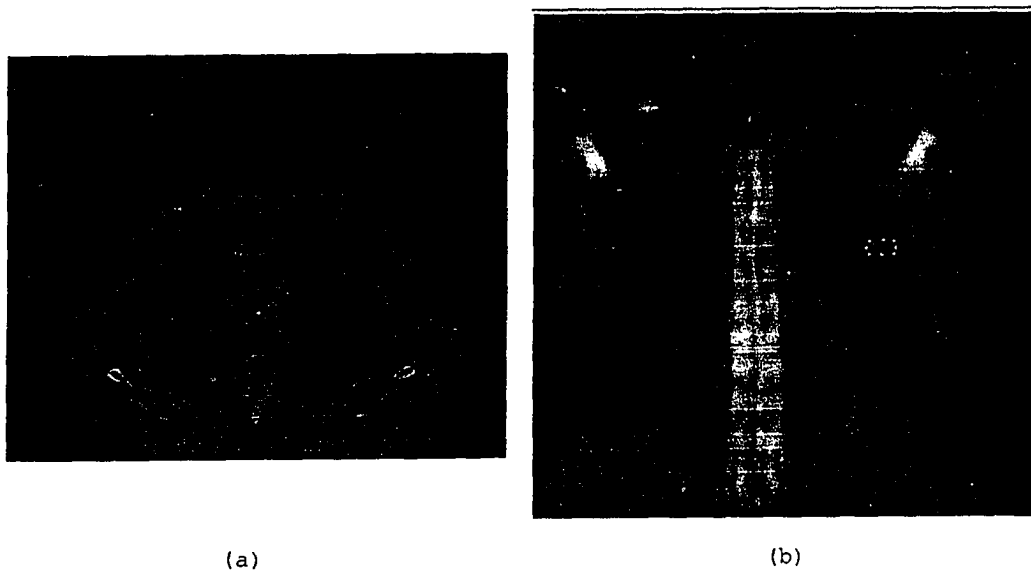


Figure 5.11: Test case 1: (a) CT slice 32 and (b) DRR reconstructed from 72 CT slices.

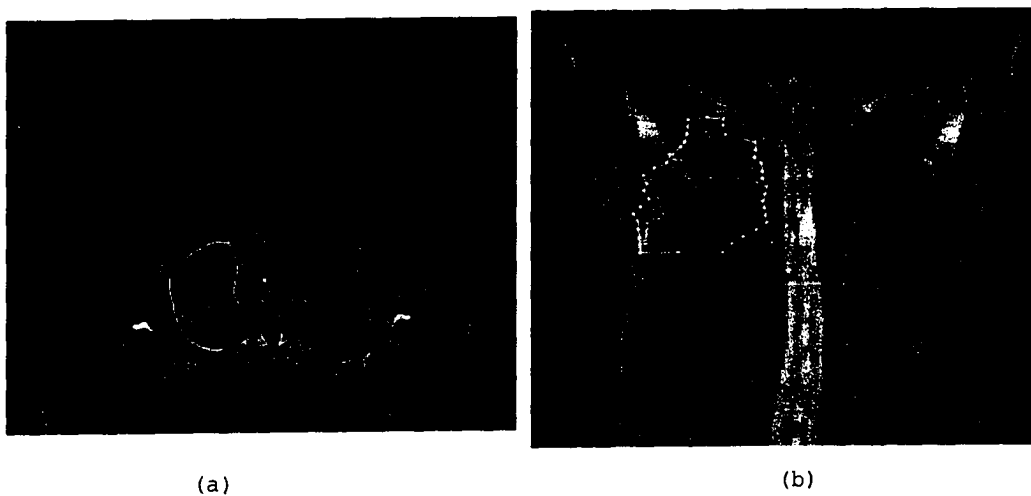


Figure 5.12: Test case 2: (a) CT slice 18 and (b) DRR reconstructed from 59 CT slices.

# Chapter 6

## Conclusion

Radiation therapy researchers always look for ways to improve the planning and delivery of radiation therapy treatments and thus improve treatment outcomes. It is known that increasing the radiation dose to the tumor increases the probability of killing the cancer. One of the goals in radiation therapy is to better control uncertainties in treatment. Thus, allowing a higher prescribed dose to be delivered to the tumor while avoiding increasing the dose to the surrounding healthy tissues.

This work addressed the tumor motion problem and its compensation solution. One of the major causes of tumor motion is patients' breathing during treatment. The errors in targeting a moving tumor can have two undesirable effects. First, if the tumor is not in the irradiated region it may receive less radiation than prescribed and risk an unsuccessful treatment. Second, if nearby critical organs are erroneously placed in the beam of radiation, they may receive a dose higher than they can tolerate and cause undesirable side effects.

We proposed a noninvasive and geometry-based solution to compensate for the tumor motion problem in radiation therapy. It is aimed at reducing the PTV safety margin during treatment planning and to monitor tumor movement during treatment. To compute tumor coverage for the purpose of reducing the PTV safety margin, we presented a path polygon algorithm, which was able to solve the following

problem: Given an  $n$ -vertex simple polygon  $P = \{v_1, v_2, \dots, v_n\}$ , a monotone chain  $C = \{c_1, c_2, \dots, c_m\}$ , compute a minimum area polygon  $Q$  that contains all the space covered by  $P$  as it is translated along  $C$  such that  $v_1 \in P$  touches  $C$ . The algorithm requires  $O(mn + m \log n \log(n + m))$  time in the worst case.

Based on the introduced solution and algorithm, a software system, which is described in Chapter 5, was developed. The system is an integrated part of the solution and is designed to be implemented as a computer assistant tool for reducing PTV safety margin. It includes the following components: DRR; ROI Projection to DRR; Image Registration; Tumor Tracing Automatically; Path Polygon Computation.

Due to the restriction of time and resources, the proposed solution has not been completely investigated and the software tool, which was developed is only the first stage to our goal. We are aware that there are still a number of aspects that need to be verified before this tool is ready for clinical use during treatment planning.

Future work will mainly focus on improving and automating the system. Some aspects being considered for the next step are:

- The computation of the DRR is a critical step in our system. In the future, we are going to work on improving its quality and on enhancing the contrast of bone structure. For the execution time, since using a ray casting algorithm involves traversal of all CT patient data voxels, it takes more than 10 minutes to reconstruct a  $512 * 512$  size DRR from 62 slices with the resolution of  $512 * 512$ . One area needing future work is to compare the existing DRR techniques and pay attention to both matters of quality and speed.

- Tumor locations in X-ray radiographs are the basis of computing tumor coverage. Currently, we are using a simple density-based method to identify a tumor automatically in X-ray radiograph. Its accuracy is affected by the radiographs' low contrast and noise. It's also not very convenient for the user to identify them in each radiograph. One of the most common techniques is to use image processing filters before automatic tumor detection.

- For the simplicity, we have assumed that the tumor shape doesn't change during

patient's breathing cycle and the period of treatment. This assumption may not always be true. One of our future work is to consider changes of tumor shape, tumor rotation, and 3D tumor movement.

- So far, we tested our system completely with only one set of patient data. The error analysis of image registration and the effectiveness of the tumor coverage to the PTV margin needs to be evaluated using additional clinical data.

# Bibliography

- [1] S. Benedict. Looking into patient positioning and organ motion. <http://www.acmp.org/meetings/hershey-2001/highlights/benedict.pdf>, 2001.
- [2] M. BERG, M. Kreveld, M. Overmars, and O. Cheong. *Computational Geometry*. Springer, 2nd edition, 2000.
- [3] L.M.G. Brown and T.E. Boult. Registration of planar film radiographs with computed tomography. *IEEE Workshop on Mathematical Methods Biomedical Imaging*, 1996.
- [4] E.L. Chaney, J.S. Thorn, G. Tracton, T. Cullip, J.G. Roseman, and J.E. Tepper. A portal software tool for computing digitally reconstructed radiographs. *Int.J.Radiation Oncology Biol.Phys*, 32(2):491–497, 1995.
- [5] C.W. Cheng, L.M. Chen, and P.K. Kijewski. A coordinate transfer of anatomical information from ct to treatment simulation. *Int.J.Radiation Oncology Biol.Phys*, 13:1559–1569, 1987.
- [6] P.C.F. Cheung, K.E. Sixel, R. Tirona, and Y.C. Ung. Reproducibility of lung tumor positions and reduction of lung mass within the planning target volume using active control (abc). *Int. J. Radiation Oncology Biol.Phys*, 57(5):1437–1442, 2003.
- [7] A.P. Dhawan. *Medical Image Analysis*. A John Wiley and models Sons, Inc., 2003.

- [8] L. Dong and A.L. Boyer. An image correlation procedure for digitally reconstructed radiographs and electronic portal images. *Int.J.Radiation Oncology Biol.Phys*, 33(5):1053–1060, 1995.
- [9] A. Ezz, P. Munro, A.T. Porter, J. Battista, D.A. Jaffray, A. Fenser, and S. Osborne. Daily monitoring and correction of radiation field placement using a video-based portal imaging system: a pilot study. *Int. J. Rad. Oncol. Biol. Phys.*, 22:159–165, 1992.
- [10] J.D. Foley, A. DAM, S.K. Feiner, and J.F. Hughes. *Computer Graphics*. Addison-Wesley, 2nd edition, 1995.
- [11] E.C. Ford, G.S. Mageras, E. Yorke, K.E. Rosenzweig, R. Wagman, and C.C. Ling. Evaluation of respiratory movement during gated radiotherapy using film and electronic protal imaging. *Int.J.Radiation Oncology Biol.Phys.*, 52(2):522–531, 2002.
- [12] J.M. Galvin, C. Sims, G. Dominiak, and J.S. Cooper. The use of digitally reconstructed radiographs for three-dimensional treatment planning and ct-simulation. *Int.J.Radiation Oncology Biol.Phys*, 31(4):935–942, 1995.
- [13] L.H. Gerg, S.F. El-Hakin, J. Szanto, D. Salhani, and A. Girard. The development and clinical application of a patient position monitoring system. In *In Videometrics iii*, SPIE 2350, Boston, MA, Nov 1994. SPIE.
- [14] S.W. Hadley. *Video-based patient positioning for external beam radiation therapy*. Doctor of philosophy, The University of Chicago, Chicago, Illinois, 2002.
- [15] R.T. Haken. Technical issues with stereotaxic radiosurgery. <http://www.webtie.org>.
- [16] J. Hanley, M.M. Debois, D. MAh, G.S. Mageras, A. Raben, K. Rosenzweig, B. Mychalczak, L.H. Schwartz, P.J. Gloeggler, W. Lutz, C.C. Ling, S.A. Leibel, Z. Fuks, and G.J. Kutcher. Deep inspiration breath-hold technique for lung

- tumors: The potential value of target immobilization and reduced lung density in dose escalation. *Int.J.Radiation Oncology Biol.Phys.*, 45(3):603–611, 1999.
- [17] T. Harada, H. Shirato, S. Ogura, S. Oizumi, K. Yamazaki, S. Shimizu, R. Onimaru, K. Miyasaka, M. Nishimura, and H. Dosaka-Akita. Real-time tumor-tracking radiation therapy for lung carcinoma by the aid of insertin of a gold marker using bronchofiberscopy. *Cancer*, 95:1720–1727, 2002.
- [18] M.G. Herman, K.O. Khadivi, L. Kleinberg, I. Gage, and R.A. Abrams. Effects of respiration on target and critical structure positions during treatment assessed with movie-loop electronic portal imaging. *Int.J.Radiation Oncology Biol.Phys.*, 39:163–169, 1997.
- [19] D.L.G. Hill, P.G. Batchelor, M. Holden, and D.J. Hawkes. Medical image registration. *Phys. Med. Biol.*, 46:R1–R45, 2001.
- [20] D.H. Hristov and B.G. Fallone. A grey-level image alignment algorithm for registration of portal images and digitally reconstruted radiographs. *Med. Phys.*, 23(1):75–84, 1996.
- [21] P.J. Keall, V.R. Kini, S.S. Vedan, and R. Mohau. Motion adaptive x-ray therapy: a feasibility study. *Phys. Med. Biol.*, 46:1–10, 2001.
- [22] J.H. Killoran, E. H. Baldini, C.J. Beard., and L. Chin. A technique for optimization of digitally reconstructed radiographs of the chest in virtual simulation. *Int.J.Radiation Oncology Biol.Phys.*, 49(1):231–239, 2003.
- [23] J.H. Killoran, H.M. Kooy, D.J. Gladstone, F.J. Welte, and C.J. Beard. A numerical simulation of organ motion and daily setup uncertainties: Implications for radiation therapy. *Int.J.Radiation Oncology Biol.Phys.*, 37(1):213–221, 1997.
- [24] V.R. Kini, S.S. Vedam, P.J. Keall, S. Patil, C. Chen, and R. Mohan. Patient training in respiratory-gated radiotherapy. *Medical Dosimetry*, 28(1):7–11, 2003.
- [25] J.R.V.S.D. Koste, H.C.J.D. Boer, R.H. Schuchhard-Schipper, S. Senan, and B.J.M. Heijmen. Procedures for high precision setup verification and correction of

- lung cancer patients using ct-simulation and digitally reconstructed radiographs (drr). *Int.J.Radiation Oncology Biol.Phys.*, 55(3):840–810, 2003.
- [26] H.D. Kubo and B.C. Hill. Respiration gated radiotherapy treatment: a technical study. *Phys. Med. Biol.*, 41:83–91, 1996.
- [27] H. Livyatan, Z. Yaniv, and L. Joskowicz. Gradient-based 2-d/3-d rigid registration of fluoroscopic x-ray to ct. *IEEE Transactions on Medical Imaging*, 22(11):1395–1406, 2003.
- [28] J.B.A. Maintz and M.A. Viergever. A survey of medical image registration. *Medical Image Analysis (1998)*, 2(1):1–37, 1998.
- [29] A.L. Mckenzie. How should breathing motion be combined with other errors when drawing margins around clinical target volumes? *The British Journal of Radiology*, 73:973–977, 2000.
- [30] M. Overmars O. Schwarzkopf M.D. Berg, M.V. Kreveld. Computational geometry: Algorithms and applications, 1998.
- [31] N. Milickovic, D. Baltas, S. Giannouli, M. Lahanas, and N. Zamboglou. Ct imaging based digitally reconstructed radiographs and its application in brachytherapy. <http://www.mlahanas.de/Papers/preprint/DRR-paper.pdf>, 2003.
- [32] S. Minohara, T. Kanai, M. Endo, K. Noda, and M. Kanazawa. Respiratory gated irradiation system for heavy-ion radiotherapy. *Int. J. Radiation Oncology Biol. Phys.*, 47(4):1097–1103, 2000.
- [33] NEMA. Digital imaging and communications in medicine. The DICOM standard: [medical.nema.org/dicom/2003.html](http://medical.nema.org/dicom/2003.html), 2003.
- [34] E. Ntasis, T.A. Maniatis, and K.S. Nikita. Fourier volume rendering for real time preview of digital reconstructed radiographs: a web-based implementation. *Computerized Medical Imaging and Graphs*, 26:1–8, 2002.

- [35] C. Ozhasoglu and M.J. Murphy. Issues in respiration motion compensation during external-beam radiotherapy. *Int. J. Radiation Oncology Biol. Phys.*, 52(5):1389–1399, 2002.
- [36] V.M. Remouchamps, F.A. Vicini, M.B. Sharpe, L.L. Kestin, A.A. Martinez, and F.W. Wong. Significant reductions in heart and lung doses using deep inspiration breath hold with active breathing control and intensity-modulated radiation therapy for patients treated with locoregional breast irradiation. *Int. J. Radiation Oncology Biol. Phys.*, 55(2):392–406, 2003.
- [37] Terry Fox Research. Canadian cancer statistics 2004. <http://www.terryfoxrun.org>.
- [38] B. Revet. *DICOM Cook Book for Implementations in Modalities*. Philips Medical Systems Nederland B.V., 1997.
- [39] K. Rosenzweig, J. Hanley, D. Mah, G. Mageras, M. Hunt, S. Toner, C. Burman, C.C. Ling, B. Mychalczak, Z. Fuks, and S.A. Leibel. The deep inspiration breath-hold technique in the treatment of inoperable non-small-cell lung cancer. *Int. J. Radiation Oncology Biol. Phys.*, 48(1):81–87, 2000.
- [40] D.B. Russakoff, T. Rohfing, R. Shahidi, D. Kim, J.R. Adler, and C.R. Maurer. Intensity-based 2d-3d spine image registration incorporating one fiducial marker. *R.E. Ellis and T.M. Peters (Eds.): MICCAI 2003, LNCS 2878*, pages 287–294, 2003.
- [41] A. Schweikard, G. Glosser, M. Bodduluri, M. Murphy, and J.R. Adler. Robotic motion compensation for respiratory movement during radiosurgery. *J. Computer-Aided Surgery*, 5(4):263–277, 2000.
- [42] G.C. Sharp, S.B. Jiang, S. Shimizu, and H. Shirato. Prediction of respiratory tumor motion for real-time image-guided radiotherapy. *Physics In Medicine and Biology*, (49):425–440, 2004.

- [43] G.W. Sherouse, K. Novins, and E.L. Chaney. Computation of digitally reconstructed radiographs for use in raditheraoy treatment design. *Int.J.Radiation Oncology Biol.Phys*, 18:651–658, 1990.
- [44] S. Shimizu, H. Shirato, S. Ogura, H. Akita-Dosaka, K. Kitamura, T. Nishioka, K. Kagei, M. Nishimura, and K. Miyasaka. Dectection of lung tumor movement in real-time tumor-tracking radiotherapy. *Int.J.Radiation Oncology Biol.Phys*, 51(2):304–310, 2001.
- [45] H. Shirato, T. Harada, T. Harabayashi, K. Hida, H. Endo, K. Kitamura, R. Onimaru, K. Yamazaki, N. Kurauchi, T. Shimizu, N. Shinohara, M. Matsushita, H. Dosaka-Akita, and K. Miyasaka. Feasibility of insertion/implantation of 2.0-mm-diameter gold internal fiducial markers for precise setup and real-time tumor tracking in radiotherapy. *Int.J.Radiation Oncology Biol.Phys*, 56(1):240–247, 2003.
- [46] H. Shirato, S. Shimizu, K. Kitamura, T. Nishioka, K. Kagei, , S. Hashimoto, H. Aoyama, T. Kunieda, N. Shinohara, H. Dosaka-Akita, and K. Miyasaka. Four-dimensional tratment planning and fluoroscopic real-time tumor tracking radiotherapy for moving tumor. *Int.J.Radiation Oncology Biol.Phys*, 48(2):435–442, 2000.
- [47] Varian Medical Systetems. Respiratory gating : Real-time position management (rpm). <http://www.varian.com/onc/prd057.html>, 2003.
- [48] International Commission On Radiation Units and Measurements. Prescribing, recording, and reporting photon beam therapy. *Technical Report 50, International Commission of Radiation Units and Measurements*, 1993.
- [49] virtualdub.org. <http://www.virtualdub.org>.
- [50] K. Weidenbach. Shooting a moving target: planning for breathing movements in radiation therapy. Technical report, Standford University, 2000.

- [51] J.W. Wong, M.B. Sharpe, D.A. Jaffray, J.M. Robertson, J.S. Stromberg, V.R. Kini, and A.A. Nartinez. The use of active breathing control (abc) to reduce margin for breathing motion. *Int.J.Radiation Oncology Biol.Phys*, 44(4):911–919, 1999.

# Appendix A

## CT Slice Information Dumping

CT2.16.124.113534.2.3.5.0.120031105.20936.353.11646.24.dcm  
(0002;0000) UL: 182  
(0002;0001) OB: 0  
(0002;0002) UI: 1.2.840.10008.5.1.4.1.1.2  
(0002;0003) UI: 2.16.124.113534.2.3.5.0.120031105.20936.353.11646.24  
(0002;0010) UI: 1.2.840.10008.1.2.1  
(0002;0012) UI: 1.2.250.1.59.3.0.3.3.1  
(0002;0013) SH: DU V3.0  
(0008;0000) UL: 308  
(0008;0008) CS: ORIGINAL\PRIMARY\AXIAL  
....  
(0020;0032) DS: -275.00\ -275.00\20.00  
(0020;0037) DS: 1.0\0.0\0.0\0.0\1.0\0.0  
(0020;0052) UI: 2.16.124.113534.2.3.5.0.120031105.20936.353.7594  
(0020;0060) CS:  
(0020;1040) LO:  
(0020;4000) LT:  
(0028;0000) UL: 136  
(0028;0002) US: 1  
(0028;0004) CS: MONOCHROME2  
(0028;0010) US: 512  
(0028;0011) US: 512  
(0028;0030) DS: 1.074219\1.074219  
(0028;0100) US: 16  
(0028;0101) US: 16  
(0028;0102) US: 15  
(0028;0103) US: 1  
(0028;1052) DS: 0  
(0028;1053) DS: 1  
(7FE0;0000) UL: 524300  
(7FE0;0010) OW: 524288



# **Appendix B**

## **RT Structure Information Dumping**

RS2.16.124.113534.2.3.5.0.120031105.20936.354.2540.dcm  
(0002;0000) UL: 182  
(0002;0001) OB: 0  
(0002;0002) UI: 1.2.840.10008.5.1.4.1.1.481.3  
(0002;0003) UI: 2.16.124.113534.2.3.5.0.120031105.20936.354.2540  
(0002;0010) UI: 1.2.840.10008.1.2.1  
(0002;0012) UI: 1.2.250.1.59.3.0.3.3.1  
(0002;0013) SH: DU V3.0  
(0008;0000) UL: 248  
(0008;0012) DA: 20031105  
(0008;0013) TM: 093654  
(0008;0016) UI: 1.2.840.10008.5.1.4.1.1.481.3  
(0008;0018) UI: 2.16.124.113534.2.3.5.0.120031105.20936.354.2540  
(0008;0020) DA: 20030721  
(0008;0030) TM: 121800  
(0008;0050) SH:  
(0008;0060) CS: RTSTRUCT  
(0008;0070) LO: XXXXXXXXXXXX  
(0008;0090) PN:  
(0008;1010) SH: XXXXXXXXXXXX  
(0008;1090) LO: TheraplanPlus  
(0010;0000) UL: 56  
(0010;0010) PN: XXXXXX,XXXXXX  
....  
(3006;0084) IS: 5  
(FFFE;E00D) : 0  
(FFFE;E000) : -1  
(3006;002A) IS: 255\0\0  
(3006;0040) SQ: -1  
(FFFE;E000) : -1  
(3006;0016) SQ: -1

(FFFE;E000) : -1  
(0008;1150) UI: 1.2.840.10008.5.1.4.1.1.2  
(0008;1155) UI: 2.16.124.113534.2.3.5.0.120031105.20936.353.11646.21  
(FFFE;E00D) : 0  
(FFFE;E0DD) : 0  
(3006;0042) CS: CLOSED\_PLANAR  
(3006;0046) IS: 33  
(3006;0050) DS: -86.58\ -3.87\35.00\ -83.74\ -3.81\35.00\ -81.64\ -4.30\...  
(FFFE;E00D) : 0  
(FFFE;E000) : -1  
(3006;0016) SQ: -1  
(FFFE;E000) : -1  
(0008;1150) UI: 1.2.840.10008.5.1.4.1.1.2  
(0008;1155) UI: 2.16.124.113534.2.3.5.0.120031105.20936.353.11646.22  
(FFFE;E00D) : 0  
(FFFE;E0DD) : 0  
(3006;0042) CS: CLOSED\_PLANAR  
(3006;0046) IS: 34  
(3006;0050) DS: -98.83\ -24.92\30.00\ -99.47\ -25.35\30.00\ -100.12\...  
(FFFE;E00D) : 0  
(FFFE;E000) : -1  
(3006;0016) SQ: -1  
(FFFE;E000) : -1  
(0008;1150) UI: 1.2.840.10008.5.1.4.1.1.2  
(0008;1155) UI: 2.16.124.113534.2.3.5.0.120031105.20936.353.11646.23  
(FFFE;E00D) : 0  
(FFFE;E0DD) : 0  
(3006;0042) CS: CLOSED\_PLANAR  
(3006;0046) IS: 42  
(3006;0050) DS: -97.75\ -39.53\25.00\ -98.61\ -36.31\25.00\ -99.90\...  
(FFFE;E00D) : 0

(FFFE;E000) : -1  
(3006;0016) SQ: -1  
(FFFE;E000) : -1  
(0008;1150) UI: 1.2.840.10008.5.1.4.1.1.2  
(0008;1155) UI: 2.16.124.113534.2.3.5.0.120031105.20936.353.11646.24  
(FFFE;E00D) : 0  
(FFFE;E0DD) : 0  
(3006;0042) CS: CLOSED\_PLANAR  
(3006;0046) IS: 41  
(3006;0050) DS: -75.62\ -2.36\20.00\ -76.05\ -5.80\20.00\ -76.48\ -7.52\...  
(FFFE;E00D) : 0  
(FFFE;E000) : -1  
(3006;0016) SQ: -1  
(FFFE;E000) : -1  
(0008;1150) UI: 1.2.840.10008.5.1.4.1.1.2  
(0008;1155) UI: 2.16.124.113534.2.3.5.0.120031105.20936.353.11646.25  
(FFFE;E00D) : 0  
(FFFE;E0DD) : 0  
(3006;0042) CS: CLOSED\_PLANAR  
(3006;0046) IS: 36  
(3006;0050) DS: -83.57\ -19.12\15.00\ -84.43\ -20.62\15.00\ -85.51\ -22.13\...  
(FFFE;E00D) : 0  
(FFFE;E000) : -1  
(3006;0016) SQ: -1  
(FFFE;E000) : -1  
(0008;1150) UI: 1.2.840.10008.5.1.4.1.1.2  
(0008;1155) UI: 2.16.124.113534.2.3.5.0.120031105.20936.353.11646.26  
(FFFE;E00D) : 0  
(FFFE;E0DD) : 0  
(3006;0042) CS: CLOSED\_PLANAR  
(3006;0046) IS: 38

(3006;0050) DS: -80.14\ -12.68\10.00\ -81.00\ -13.96\10.00\ -81.86\ -15.47\...

....

# **Appendix C**

## **RT Plan Information Dumping**

RP2.16.124.113534.2.3.5.0.120031105.20936.355.6905.dcm  
(0002;0000) UL: 182  
(0002;0001) OB: 0  
(0002;0002) UI: 1.2.840.10008.5.1.4.1.1.481.5  
(0002;0003) UI: 2.16.124.113534.2.3.5.0.120031105.20936.355.6905  
(0002;0010) UI: 1.2.840.10008.1.2.1  
(0002;0012) UI: 1.2.250.1.59.3.0.3.3.1  
(0002;0013) SH: DU V3.0  
(0008;0000) UL: 254  
(0008;0012) DA: 20031105  
(0008;0013) TM: 093657  
(0008;0016) UI: 1.2.840.10008.5.1.4.1.1.481.5  
(0008;0018) UI: 2.16.124.113534.2.3.5.0.120031105.20936.355.6905  
(0008;0020) DA: 20030721  
(0008;0030) TM: 121800  
(0008;0050) SH:  
(0008;0060) CS: RTPLAN  
(0008;0070) LO: XXXXXXXXXXXX  
(0008;0090) PN:  
(0008;1010) SH: XXXXXXXXXXXX  
(0008;1070) PN:  
(0008;1090) LO: TheraplanPlus  
(0010;0000) UL: 56  
(0010;0010) PN: XXXXXX,XXXXXX  
(0010;0020) LO: 02-036857  
(0010;0030) DA:  
(0010;0040) CS:  
(0018;0000) UL: 16  
(0018;1020) LO: DU V3.0  
(0020;0000) UL: 150  
(0020;000D) UI: 2.16.124.113534.2.3.5.0.120031105.20936.353.18727

(0020;000E) UI: 2.16.124.113534.2.3.5.0.120031105.20936.353.19566  
(0020;0010) SH: 20030721:121800  
(0020;0011) IS: 1  
(3005;0000) UL: 68  
(3005;0010) LO: XXX XXXXXXX CALCULATION  
(3005;1008) CS: NONE  
(3005;100A) CS: TO\_BE\_CALCULATED  
(300A;0000) UL: 3914  
(300A;0002) SH: INITIAL 3 FIELDS  
(300A;0003) LO: INITIAL 3 FIELDS  
(300A;0006) DA: 20030728  
(300A;0007) TM: 104923  
(300A;000C) CS: PATIENT  
(300A;0070) SQ: -1  
(FFFE;E000) : -1  
(300A;0071) IS: 1  
(300A;0078) IS: 25  
(300A;0080) IS: 3  
(300A;00A0) IS: 0  
(300C;0004) SQ: -1  
(FFFE;E000) : -1  
(300A;0086) DS: 103  
(300C;0006) IS: 1  
(FFFE;E00D) : 0  
(FFFE;E000) : -1  
(300A;0086) DS: 116  
(300C;0006) IS: 2  
(FFFE;E00D) : 0  
(FFFE;E000) : -1  
(300A;0086) DS: 124  
(300C;0006) IS: 3

(FFFE;E00D) : 0  
(FFFE;E0DD) : 0  
(300C;006A) IS: 1  
(FFFE;E00D) : 0  
(FFFE;E0DD) : 0  
(300A;00B0) SQ: -1  
(FFFE;E000) : -1  
(300A;00B2) SH: 6 MV MLC  
(300A;00B3) CS: MU  
(300A;00B4) DS: 1000.00  
(300A;00B6) SQ: -1  
(FFFE;E000) : -1  
(300A;00B8) CS: ASYMX  
(300A;00BC) IS: 1  
(FFFE;E00D) : 0  
(FFFE;E000) : -1  
(300A;00B8) CS: ASYMY  
(300A;00BC) IS: 1  
(FFFE;E00D) : 0  
(FFFE;E000) : -1  
(300A;00B8) CS: MLCX  
(300A;00BC) IS: 29  
(300A;00BE) DS: -200.00\ -135.00\ -125.00\ -115.00\ -105.00\ -95.00\ -85.00\ ...  
(FFFE;E00D) : 0  
(FFFE;E0DD) : 0  
....